

# **Master's Thesis**

## **Characterization of filtered Cathodic Arc Plasma Processes**

### **Focusing on Mass Spectroscopy and Ion Flux measurements**

Investigation of correlation between ion flux and deposition rate  
for TiAl and TiAlN thin films

#### **Author**

Paul Junk

#### **Supervisors**

Dr. Yeliz Unutulmazsoy

Dr. Dmitry Kalanov

#### **Institution**

Leibniz Institute of Surface Engineering (IOM)

Leipzig University

#### **Submission Date**

December 3, 2025

---

## Contents

---

<b>1</b>	<b>Introduction and Literature Review</b>	<b>6</b>
1.1	Motivation and Industrial Context . . . . .	6
1.2	State of the Art . . . . .	7
1.3	Objectives and Approach . . . . .	7
<b>2</b>	<b>Theoretical Background</b>	<b>9</b>
2.1	Plasma Generation and Composition . . . . .	9
2.1.1	Cathode Spot Plasma Generation . . . . .	9
2.1.2	Plasma Composition and Expansion . . . . .	10
2.2	Ion Energy and Flux . . . . .	11
2.2.1	Ion Energies: Origins and Implications . . . . .	11
2.2.2	Ion Flux and Diagnostics . . . . .	11
2.3	Plasma–Surface Interactions and Film Growth . . . . .	13
2.3.1	Energetic Condensation and Subplantation . . . . .	13
2.3.2	Reactive vs Metallic Mode . . . . .	13
2.4	Crystal Structure and Densification . . . . .	14
2.4.1	Structure-Zone Models . . . . .	14
2.4.2	TiAlN Crystal Structures . . . . .	15
<b>3</b>	<b>Experimental Methodology</b>	<b>17</b>
3.1	Experimental Apparatus and Setup . . . . .	17
3.1.1	Vacuum & Gas Infrastructure . . . . .	17
3.1.2	Power & Triggering . . . . .	18
3.2	In situ Diagnostics . . . . .	20
3.2.1	Ion-current Probe- Langmuir probe . . . . .	20
3.2.2	Quartz Crystal Microbalance . . . . .	21

3.2.3	Comparability with QCM Measurements . . . . .	22
3.2.4	Quadrupole Mass Spectrometer . . . . .	23
3.3	Ex situ Measurements . . . . .	25
3.3.1	X-ray Diffraction (XRD) . . . . .	25
3.3.2	X-ray Reflectometry (XRR) . . . . .	26
3.3.3	Scanning Electron Microscopy (SEM) . . . . .	26
3.3.4	Energy-dispersive X-ray spectroscopy (EDX) . . . . .	26
3.3.5	Profilometry . . . . .	26
3.4	Data Processing . . . . .	27
3.5	Error Handling . . . . .	27
3.5.1	Mass Spectrometry Measurements . . . . .	27
3.5.2	QCM and Ion Current Probe Measurements . . . . .	28
3.5.3	Error Propagation Analysis . . . . .	29
<b>4</b>	<b>Results</b>	<b>31</b>
4.1	Langmuir Probe Bias Voltage Characterization . . . . .	31
4.1.1	Validation of Langmuir Probe Operation . . . . .	31
4.1.2	Analysis of the Ion Saturation Curve . . . . .	32
4.1.3	Selection of Operating Bias Voltage . . . . .	33
4.1.4	Ion current Variation over different pulses . . . . .	33
4.2	Quartz crystal Microbalance and Ion current Probe . . . . .	34
4.2.1	Metallic Case (No Nitrogen) . . . . .	36
4.2.2	Distance as a variable . . . . .	37
4.2.3	Magnetic Field as a variable . . . . .	38
4.2.4	Nitrogen pressure as a variable . . . . .	39
4.3	Mass spectrometry Results . . . . .	39
4.4	Ex situ Results . . . . .	41
4.4.1	Profilometry . . . . .	41
4.4.2	XRD . . . . .	41
4.4.3	XRR . . . . .	41
4.4.4	EDX . . . . .	41
4.5	Fluxes . . . . .	41
<b>5</b>	<b>Discussion of Results</b>	<b>42</b>
<b>6</b>	<b>Conclusion</b>	<b>43</b>
<b>7</b>	<b>final words or smt like thanks everyone</b>	<b>44</b>
<b>A</b>	<b>Additional Plots</b>	<b>45</b>



## Abstract

Pulsed filtered cathodic arc deposition generates highly ionized metal plasmas capable of producing dense, crystalline thin films without substrate heating. However, the process involves multiple coupled parameters: external magnetic fields simultaneously increase both ion charge states (potential energy) and ion flux, while reactive gases alter plasma composition through charge-exchange collisions. This thesis investigates the individual roles of ion flux and ion energy in Ti–Al–N thin film growth by systematically varying magnetic field strength (0–0.25 T), nitrogen pressure (0–0.3 Pa), and spatial position (10–20 cm from the plasma source).

Two diagnostics were operated simultaneously: a Langmuir probe measured ion current density, a quartz crystal microbalance tracked deposited mass. Additionally an energy-resolving mass spectrometer determined charge-state-resolved ion energy distributions. Measurements were performed in both metallic mode (vacuum) and reactive mode (nitrogen background) to characterize the transition between regimes.

The results show that increasing the magnetic field strength can amplify ion flux by up to a factor of eight. In reactive mode, the presence of nitrogen further boosts ion flux, as charge-exchange collisions reduce the number of highly ionized species and increase the proportion of lower-ionization ions. Energy-resolved mass spectrometry shows the charge-state distribution shifts toward lower ionization levels when operating in reactive mode. It also confirms that the total ion energy (kinetic and potential energy) remains within the 30–70 eV range, which is ideal for room-temperature crystallization.

This work extends the energy-flux decoupling framework established for (V,Al)N coatings to the industrially relevant TiAlN system and demonstrates that ion flux control via magnetic field strength provides a viable route to tailoring film microstructure independently of substrate temperature.

# CHAPTER 1

---

## Introduction and Literature Review

---

### 1.1 Motivation and Industrial Context

Titanium aluminum nitride ( $\text{Ti}_{1-x}\text{Al}_x\text{N}$ ) coatings are widely used in cutting tools and wear-resistant applications because of their high hardness (25–35 GPa), thermal stability, and oxidation resistance [22]. These properties depend on maintaining the metastable cubic B1 crystal structure, which provides superior mechanical performance compared to the thermodynamically stable wurtzite phase [19]. Traditional deposition methods require substantial substrate heating to achieve dense, crystalline coatings. Cathodic arc deposition offers a key advantage: highly ionized metal plasmas with intrinsic ion energies of 50–80 eV enable room-temperature crystallization through energetic condensation [3].

The challenge is that cathodic arc processes involve multiple coupled parameters. Ion energy has two components: kinetic energy from plasma expansion and potential energy released upon neutralization. The ion flux determines how rapidly this energy is delivered to the growing film. External magnetic fields can enhance both ion charge states and flux by up to an order of magnitude [5], while adding reactive gases such as nitrogen introduces charge-exchange collisions that alter plasma composition [3]. Understanding how these parameters individually influence film properties remains a fundamental challenge for predictive process control.

## 1.2 State of the Art

Recent systematic studies have made progress in understanding ion energy effects in cathodic arc deposition. Unutulmazsoy et al. showed that applying an external magnetic field to the cathode increases ion charge states (and thus potential energy), while applying a DC bias to the arc source adjusts kinetic energy [28]. Their work on (V,Al)N films demonstrated that crystalline coatings can be achieved at room temperature when the total ion energy exceeds a threshold value. Kalanov et al. refined this approach using detailed energy-resolved mass spectrometry, confirming that film crystallinity correlates more strongly with total ion energy ( $E_{\text{kin}} + E_{\text{pot}}$ ) than with either component alone [15].

Both studies identified a critical limitation: the magnetic field not only modifies ion energy but also increases ion flux by a factor of up to 10. As Unutulmazsoy et al. noted, "application of an external magnetic field also leads to an enhancement of the ion flux and hence the desired complete decoupling of the potential and kinetic energy effects will require further steps" [28]. The role of ion flux as an independent variable affecting energy delivery rate, adatom mobility, and nucleation kinetics has not been systematically investigated.

These studies also focused primarily on metallic mode (vacuum deposition), leaving the transition to reactive mode largely unexplored. Adding nitrogen fundamentally alters plasma composition through cathode poisoning, charge-exchange collisions, and generation of nitrogen ion species ( $\text{N}^+$ ,  $\text{N}_2^+$ ) [3, 6]. For TiAlN specifically, while comparative studies between cathodic arc and magnetron sputtering have shown that ion energy flux significantly affects texture and mechanical properties [16], the flux-energy decoupling framework established for (V,Al)N has not been applied to this industrially important system. No systematic study has correlated ion current density (Langmuir probe), deposited mass (QCM), and film structure across the parameter space of magnetic field strength, nitrogen pressure, and spatial position.

## 1.3 Objectives and Approach

This thesis addresses these gaps by systematically investigating the role of ion flux in Ti-Al-N thin film growth via pulsed filtered cathodic arc deposition. The specific objectives are:

1. Characterize ion flux as a function of external magnetic field strength (0–0.25 T) using Langmuir probe measurements while simultaneously measuring mass deposition via QCM. Furthermore measure the ion energy distributions via energy-resolved mass spectrometry (ERMS).

2. Investigate the transition from metallic to reactive mode by varying nitrogen pressure (0–0.3 Pa) and quantify how this affects the ion to neutral arrival ratio and charge-state distributions.
3. Establish quantitative correlations between ion current, deposited mass (via QCM) across the experimental parameter space of magnetic field, nitrogen pressure, and distance from the macroparticle filter.
4. Characterize the crystal structure (XRD), the film thickness (Profilometry), the film composition (EDX) and microstructure (XRR/SEM) of deposited TiAlN films to correlate plasma parameters with film properties.

The experimental approach combines three diagnostics: a biased Langmuir probe measures ion current density, a quartz crystal microbalance tracks mass deposition, and an energy-resolving quadrupole mass spectrometer determines charge-state-resolved ion energy distributions. This multi-diagnostic strategy, applied across a systematic parameter space, **enables smt xddd**

# CHAPTER 2

---

## Theoretical Background

---

### 2.1 Plasma Generation and Composition

#### 2.1.1 Cathode Spot Plasma Generation

Cathodic-arc plasmas form at microscopic emission centers, known as cathode spots, on an otherwise cold metal electrode under vacuum. Spot ignition occurs when the local cathode surface, through breakdown of adsorbates or field-enhanced thermionic emission, undergoes a rapid, explosive release of electrons and vaporized metal. During a single spot pulse, a few nanograms of the cathode material rapidly heat up, vaporize, and ionize, producing a dense, quasineutral plasma plume composed mostly of metal ions and electrons. The peak spot current densities reach  $10^{10}$ – $10^{12} \text{ A m}^{-2}$ , far above steady-state thermionic or field emission limits. These microexplosions, termed ectons (explosive electron emission centers), produce localized nanosecond-scale plasma bursts. The arc is sustained by repetitive ecton events occurring at or near the same location [3, Chap. 3.3–3.4].

Key Characteristics of Spot-Generated Plasma:

- High degree of ionization: >90 % of the ejected metal atoms emerge as ions, a consequence of the extreme power density in the cathode spot [3, Chap. 3.5].
- Multiply charged ions: the charge state distributions extend to  $Q = 3\text{--}4$  for refractory metals, such as Ti and Al, due to the high electron temperature and density in the spot plasma [3, Chap. 3.5].
- Transient, localized heating: the sub- $\mu\text{m}$ , sub-100 ns pulse produces “atomic-scale heating”, where the energy of individual ions is deposited in a highly localized

region upon impact, influencing film growth and microstructure [3, Chap. 3.6].

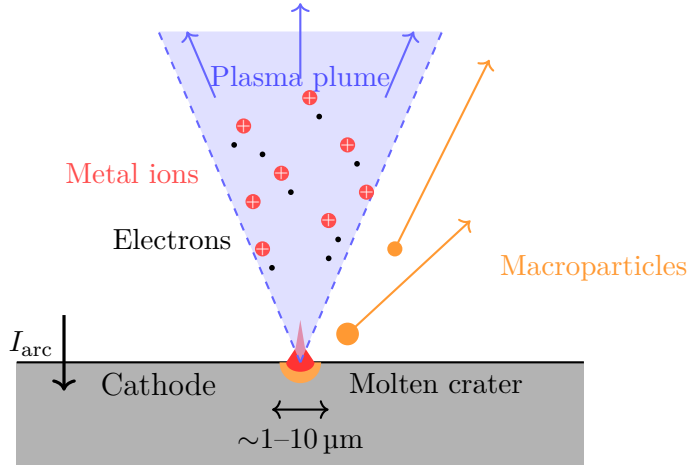


Figure 2.1: Schematic of cathode spot operation. The arc current  $I_{\text{arc}}$  concentrates at a microscopic spot ( $1\text{--}10\ \mu\text{m}$  diameter), creating a molten crater from which a plasma plume of metal ions, electrons and macroparticles expand. Adapted from [14]

Spot ignition and quenching occur on timescales of 10–100 ns, with each pulse ejecting a fully ionized burst of metal vapour. The sustained arc discharge thus consists of continuously overlapping microplasma pulses, producing a metal-rich, high-flux ion stream well-suited for energetic thin-film deposition.

### 2.1.2 Plasma Composition and Expansion

After generation at the cathode spots, the metal-rich plasma expands into the vacuum chamber, typically passing through a magnetic macroparticle filter that removes molten droplets while guiding ions along curved field lines. In the region near the cathode (within a few centimeters of the spot), plasma densities are on the order of  $10^{18}\ \text{cm}^{-3}$  and electron temperatures  $T_e \approx 5\text{--}10\ \text{eV}$ . As the plume propagates, its density decreases according to

$$n(r) = \frac{C I_{\text{arc}}}{r^2} \quad (2.1)$$

where  $I_{\text{arc}}$  is the arc current,  $r$  the distance, and  $C$  a constant related to the ion-erosion rate of the cathode material. This  $\frac{1}{r^2}$  scaling assumes free expansion, but deviations can occur due to magnetic fields, collisions, or reactive gases, which may alter the plasma trajectory or cause recombination [3, Chap. 4.3; Eq. 4.3, p. 178].

In cathodic arc discharges from titanium cathodes, whether pure Ti or Ti-Al compounds, ions generally carry an average charge state  $\langle Q \rangle \approx 2.1\text{--}2.2$ , at the source [3, Chap. 4.1; App. B.8]. This high degree of ionization reflects the extreme power density

of the spot and follows the cohesive energy rule, which links  $\langle Q \rangle$  to the cohesive energy of the cathode material [3, App. B.8].

## 2.2 Ion Energy and Flux

### 2.2.1 Ion Energies: Origins and Implications

Ion energies in cathodic arc plasmas have been extensively characterized through time-of-flight measurements. For the materials relevant to this work both exceeding the  $\approx 30$  eV threshold for subplantation when combining the kinetic and potential energy as can be seen in Table 2.1. This enables densification and improved crystallinity in Ti–Al–N films without requiring external substrate heating [3, Chap. 8.1–8.2].

Table 2.1: Characteristic ion properties for Ti and Al cathodic arc plasmas in vacuum, near the cathode [3, App. B; Table B.8].

Species	$\langle Q \rangle$	$E_{\text{kin}}$ (eV)	$E_{\text{pot}}$ (eV)	$E_{\text{tot}}$ (eV)
Ti <sup>2+</sup>	2.1	59	21	80
Al <sup>2+</sup>	1.7	28	24	52

While ion energy influences film properties, this work focuses on quantifying the flux of both metal ions and reactive nitrogen species to understand their combined role in film growth. In metallic mode, the narrow energy distribution simplifies flux measurements and enables direct correlation with deposition rate. In reactive mode, collisions with N<sub>2</sub> broaden the energy distribution and generate additional species, N<sup>+</sup>, N<sub>2</sub><sup>+</sup>, and metastable N<sub>2</sub>, that must be distinguished in mass spectrometer measurements [6].

To isolate the effects of ion flux and reactive nitrogen, we systematically vary the N<sub>2</sub> pressure and adjust the magnetic field strength, ensuring that changes in film properties reflect controlled variations in plasma composition rather than incidental energy shifts.

### 2.2.2 Ion Flux and Diagnostics

The ion flux  $\Gamma$  represents the number of ions arriving per unit area per unit time, expressed in ions cm<sup>-2</sup> s<sup>-1</sup>. In a multiply charged plasma, the total measured ion current density  $J_i$  (A cm<sup>-2</sup>) relates to  $\Gamma$  via

$$\Gamma = \frac{J_i}{e \langle Q \rangle}, \quad (2.2)$$

where  $e$  is the elementary charge and  $\langle Q \rangle$  the average ion charge state. This relationship is central to correlating time-averaged ion flux with deposited mass.

To compare ion fluxes across different materials and arc currents, the particle system coefficient

$$k_{\text{part}} = \frac{I_i}{\langle Q \rangle I_{\text{arc}}} \quad (2.3)$$

normalizes the measured probe current  $I_i$  by the arc current  $I_{\text{arc}}$  and accounts for variations in  $\langle Q \rangle$  [3, Chap. 6.5]. This normalization is necessary because the probe measures electrical current rather than particle flux, and multiply charged ions contribute proportionally more current per particle.

In vacuum cathodic arcs, the burning voltage remains nearly constant at 30–35 V for arc currents up to 1 kA, so the plasma generation rate and thus  $\Gamma$  increases approximately linearly with  $I_{\text{arc}}$  [3, Chap. 6.5]. External magnetic fields can increase  $\Gamma$  by up to an order of magnitude by confining the plasma and prolonging ion residence time near the cathode.

The relationship between ion flux and film growth rate is given by

$$R = \frac{m_{\text{ion}} \Gamma S}{\rho_{\text{film}}}, \quad (2.4)$$

where  $m_{\text{ion}}$  is the average ion mass,  $S$  the sticking coefficient, and  $\rho_{\text{film}}$  the film density. The sticking coefficient  $S$  represents the probability that an arriving ion incorporates into the growing film rather than being reflected or resputtered; for metal ions at moderate energies (below the resputter threshold of  $\sim 100$ –200 eV),  $S \approx 1$ .

For constant ion energy and a sticking coefficient equal to one, the deposition rate scales linearly with ion flux. Deviations from linearity indicate that additional processes (such as densification, resputtering, or adatom crowding) influence film growth. Unutulmazsoy et al. observed this linear scaling in (V,Al)N films deposited by pulsed filtered cathodic arc, with deviations emerging at high flux densities where ion-induced densification becomes significant [28].

Experimentally, ion flux is determined from biased probe measurements operating in ion saturation mode, while charge-state and energy distributions are obtained via energy-resolved mass spectrometry. The diagnostic methods used in this work are described in Chapter 3.

## 2.3 Plasma–Surface Interactions and Film Growth

### 2.3.1 Energetic Condensation and Subplantation

When metal ions with sufficient energy strike the growing film, they penetrate below the surface and deposit energy through a shallow collision cascade. This subplantation process produces two key effects:

- **Localized densification:** Ions with energies above 30 eV implant beneath the surface, occupying interstitial sites and displacing near-surface atoms through knock-on collisions. This reduces porosity and increases film density, which is particularly important for transition-metal nitride coatings such as Ti–Al–N [3, Chap. 8.1].
- **Atomic-scale heating:** The deposition of kinetic energy and release of potential energy (ionization enthalpy) generate localized, nanosecond-scale temperature spikes. These enhance adatom mobility and promote crystallite coalescence without requiring global substrate heating [3, Chap. 8.2].

As  $E_{\text{kin}}$  and  $E_{\text{pot}}$  increase, films transition from porous, amorphous structures to dense, crystalline coatings. This densification introduces compressive stresses of several GPa through atomic peening [3, Chap. 8.1–8.4]. For example, TiN films grown with total ion energies of approximately 60 eV develop a preferred cubic (111) texture and hardness exceeding 30 GPa.

In cathodic arc deposition, the ion energies are primarily determined by the cathode material and plasma expansion conditions. The present work therefore focuses on characterizing the correlation between ion flux  $\Gamma$  (measured by a biased collector probe) and deposition rate (measured by QCM), rather than systematic variation of ion energy. The results of these measurements are presented in Chapter 4.

### 2.3.2 Reactive vs Metallic Mode

Cathodic arc deposition operates in two distinct regimes. In metallic mode, the cathode surface remains uncovered and the plasma consists exclusively of metal ions, characterized by high ionization degrees in the plasma. In reactive mode, a background gas such as N<sub>2</sub> adsorbs onto the cathode surface, forming a compound layer that poisons the cathode and alters both spot behaviour and plasma composition [3, Chap. 9.2].

When N<sub>2</sub> is introduced, a dynamic equilibrium develops between compound formation, through adsorption and reaction at the cathode surface and compound removal

via explosive ejection events that eject both metal and nitride fragments [3, Chap. 9.3]. The equilibrium position depends on gas pressure, arc current, and cathode composition. At low  $N_2$  pressures or high power densities, type-2 (metal-rich) spots prevail, maintaining predominantly metal ion flux. At higher pressures, type-1 (poisoned) spots dominate, producing a mixed plasma of metal and nitrogen ions [3, Chap. 9.4].

Reactive mode affects both plasma diagnostics and film growth:

- The measured probe current includes contributions from  $N^+$  and  $N_2^+$  in addition to metal ions, requiring mass-resolved analysis to separate species.
- Charge exchange with  $N_2$  reduces the average charge state of metal ions and introduces gas-ion species, altering the potential energy allocation [3, Chap. 9.4].
- Collisions during plasma expansion reduce ion drift velocities, lowering kinetic energy before substrate impact [3, Chap. 9.4].

In the present experimental setup,  $N_2$  is introduced via a ring manifold inlet downstream of the magnetic filter, minimizing pressure gradients and enabling reproducible reactive-mode operation. By comparing measurements in vacuum and under varying  $N_2$  pressures, this work investigates how reactive mode influences  $\Gamma$  and  $\langle Q \rangle$ , and how these parameters correlate with deposited mass and film composition.

## 2.4 Crystal Structure and Densification

### 2.4.1 Structure-Zone Models

The microstructure of thin films deposited by physical vapour deposition depends strongly on the energy and flux of incident species. Thornton's structure-zone model, originally developed for magnetron sputtering, relates film morphology to the homologous temperature  $T/T_m$  (substrate temperature normalized to the melting point) and working gas pressure [27]. At low  $T/T_m$  and high pressures, films exhibit porous, columnar structures (Zone 1) due to limited adatom mobility. As  $T/T_m$  increases, denser columnar (Zone T) and eventually equiaxed crystalline structures (Zone 2 and Zone 3) develop.

Anders extended this framework to account for the energetic ion bombardment characteristic of cathodic arc deposition [2]. In the revised model, ion energy  $E^*$  (normalized to a displacement energy) replaces gas pressure as the second axis, reflecting the dominant role of ion bombardment in densification. High-energy ions can induce subplantation and atomic peening even at low substrate temperatures, enabling dense, crystalline films without external heating, which is a key advantage of cathodic arc

processes. However, excessive ion energy leads to lattice damage, defect accumulation, and eventually amorphization or resputtering, defining an optimal energy window for film growth [3, Chap. 8.3].

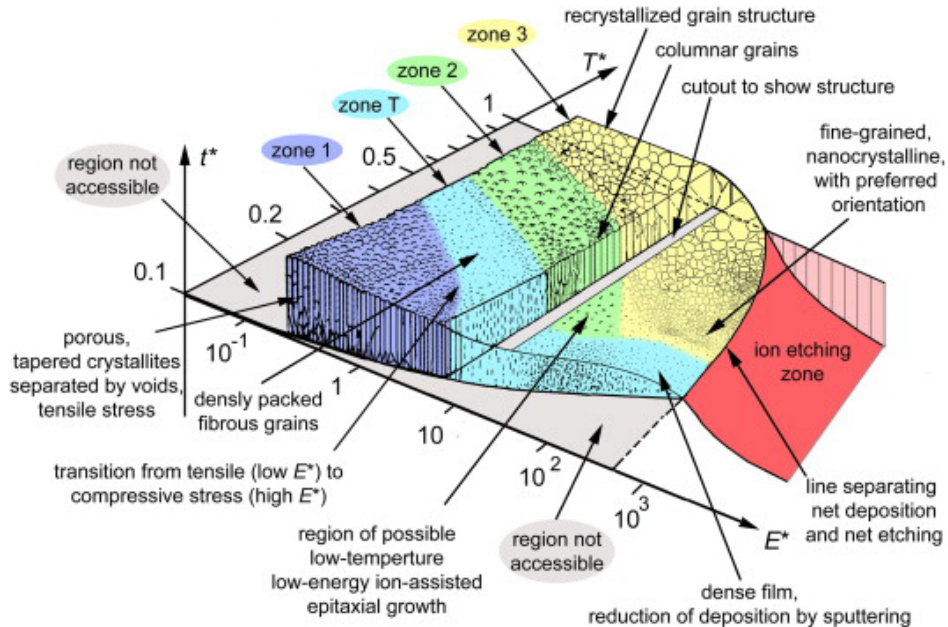


Figure 2.2: Structure-zone diagram for plasma-based thin film deposition, showing film microstructure as a function of generalized temperature  $T^*$  and normalized ion energy  $E^*$ . From Anders [2].

For the Ti–Al–N system, the Anders structure-zone model predicts that the multiply charged ions typical of cathodic arcs promote Zone T or Zone 2 microstructures even at modest substrate temperatures, provided the ion flux is sufficient to maintain a high ion-to-neutral arrival ratio.

## 2.4.2 TiAlN Crystal Structures

Titanium aluminium nitride ( $\text{Ti}_{1-x}\text{Al}_x\text{N}$ ) coatings are widely used for wear protection and cutting tools due to their high hardness, oxidation resistance, and thermal stability. The crystal structure depends primarily on the aluminium content  $x$ :

- For  $x \lesssim 0.6 - 0.7$ ,  $\text{Ti}_{1-x}\text{Al}_x\text{N}$  crystallizes in the metastable cubic B1 structure, where Al atoms substitute for Ti on the metal sublattice. This cubic phase exhibits hardness values of 25–35 GPa and is the preferred structure for most industrial applications [22].
- For  $x \gtrsim 0.7$ , the thermodynamically stable wurtzite (B4) structure becomes dominant. The wurtzite phase has lower hardness (typically 15–20 GPa) and is generally undesirable for hard coating applications [19].

- At intermediate compositions, mixed cubic-wurtzite structures or nanocomposite arrangements may form, depending on deposition conditions.

The metastable cubic phase is retained at high Al contents through kinetic limitations during low-temperature deposition. Energetic ion bombardment in cathodic arc processes can extend the solubility limit of Al in the cubic phase by providing additional energy for atomic rearrangement without the diffusion lengths associated with thermal equilibration [24].

The cathode composition used in this work (75 wt.% Ti – 25 wt.% Al is expected to produce cubic-phase  $\text{Ti}_{1-x}\text{Al}_x\text{N}$  films under typical cathodic arc conditions. Film structure will be verified by X-ray diffraction, with microstructure examined by scanning electron microscopy, as described in Chapter 3.3.

# CHAPTER 3

---

## Experimental Methodology

---

### 3.1 Experimental Apparatus and Setup

#### 3.1.1 Vacuum & Gas Infrastructure

The chamber was evacuated using a two-stage pumping system consisting of a turbo-molecular pump (backed by a rotary vane pump for initial roughing) and a cryogenic pump, achieving a base pressure on the order of  $1 \times 10^{-5}$  Pa. Nitrogen gas ( $N_2$ , 99.999% purity) was introduced via a mass flow controller (MFC), with chamber pressures ranging from 0.025–0.3 Pa during experiments,

Plasma was generated using a water-cooled anode and a cathode with the aforementioned composition of 75 wt% Ti; 25 wt% Al (62.8 at%; Ti 37.2 at% Al) with a diameter of 6.35 mm and 38.1 mm long. The arc power supply operated in pulsed DC mode, delivering up to 450 A at a pulse frequency of 0.2–5 Hz, as well as powering the 90° curved macroparticle filter in series. An accelerator coil (EM-coil), capable of currents up to 850 A, was pulsed 200  $\mu$ s before arc ignition, to stabilize the magnetic field. The QCM and Langmuir probe were mounted on a custom movable block at 10–20 cm from the filter exit, while the energy-resolving mass spectrometer (ERMS) was positioned using a linear feedthrough for external adjustment. Depositions were done with another movable mount and positioned at the necessary distances to the filter exit.

The vacuum chamber setup for cathodic arc plasma diagnostics and thin film deposition is shown in Figure 3.1. The arc power supply generates and steers the plasma, while the EM-coil power supply enhances the plasma energy and confinement.

The green arrow illustrates the trajectory of the plasma plume as it is expanding from the cathode, passing through the macroparticle filter, and reaching the diagnostics.

An energy-resolving mass spectrometer (ERMS) analyzes the ion energy and mass distribution, with its position adjusted relative to the macroparticle filter, to study spatial variations in the plasma plume. A Langmuir probe measures the ion current and a quartz crystal microbalance (QCM) monitors the deposited mass. An oscilloscope records time-resolved electrical signals: channels 1 and 2 measure the voltage drop at the cathode, while channels 3 and 4 capture the current supplied to the arc and EM-coil, as well as the ion current collected by the probe on another channel. The delay generator acts as a master clock, triggering the arc power supply, EM-coil activation, and diagnostic tools with precise timing to ensure that ion flux, energy, and deposition rate measurements are directly comparable and time-correlated.

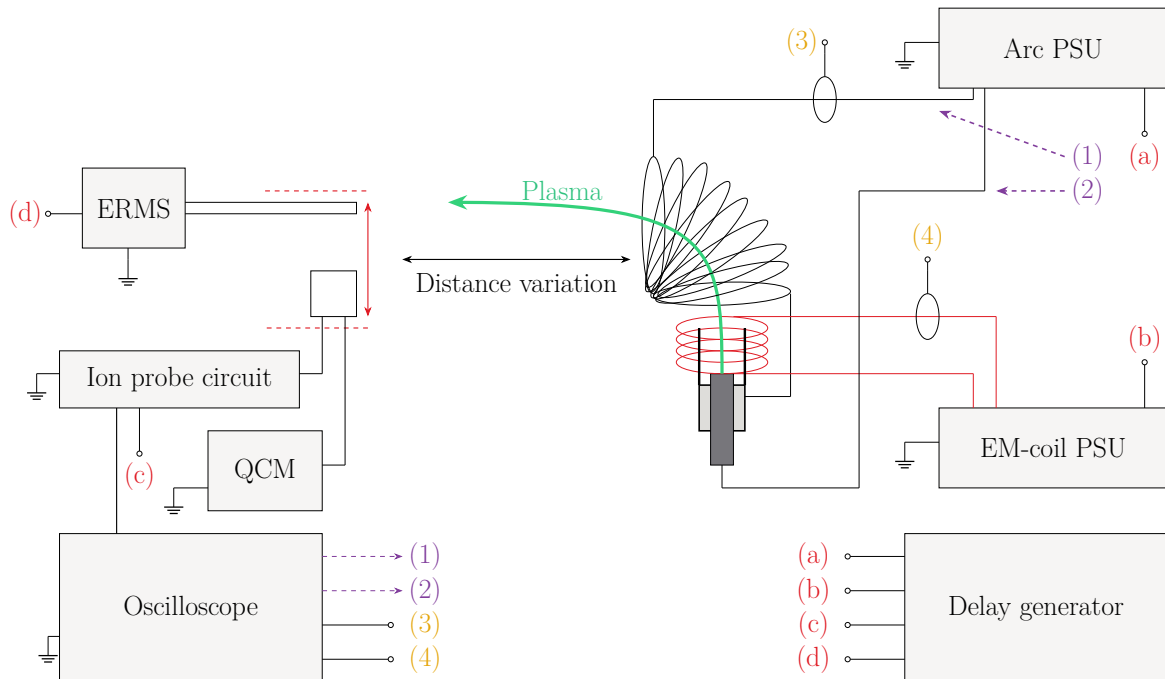


Figure 3.1: Schematic of the vacuum chamber setup for cathodic arc plasma diagnostics and thin film deposition. (a) Arc power supply, (b) EM-coil power supply, (c) Langmuir probe and QCM, (d) energy-resolving mass spectrometer (ERMS). The delay generator (a-d) synchronizes the arc power supply, EM-coil activation, and diagnostic tools.

### 3.1.2 Power & Triggering

The arc power supply operated in pulsed mode at frequencies between 0.2–5 Hz with a pulse width of 1 ms. The EM-coil was activated 200  $\mu$ s before arc ignition and lasts 1.5 ms, to ensure steady-state magnetic field conditions. A delay generator (SRS

DG645) served as the master clock, distributing triggers to:

- the arc power supply (channel **a**),
- the EM-coil power supply (channel **b**),
- the diagnostics (ERMS, QCM, and Langmuir probe; channels **c–d**).
- the oscilloscope is triggered on the rising edge of the arc power supply unit (PSU) voltage (Channel **(1)**)

This setup enabled time-resolved measurements of ion flux and energy, fully synchronized with plasma generation.

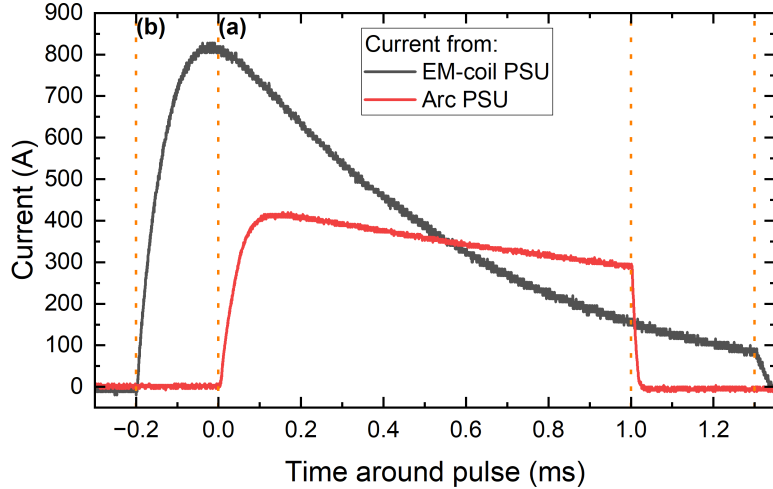


Figure 3.2: Example Pulse waveform with the triggering timings (a) and (b) for the Arc-PSU and the EM-coil PSU marked with the orange dashed line

To approximate the magnetic field generated within the EM-coil solenoid, the following equation was utilized:

$$B = \frac{\mu_0 N I}{L} \quad (3.1)$$

with the length of the solenoid  $L = 0.02\text{m}$ , the number of turns in the solenoid  $N = 5$  and the vacuum permeability  $\mu_0 = 1.256 \cdot 10^{-6} \frac{T \cdot m}{A}$ . The electrical current value was determined by the peak current recorded with the oscilloscope, typically observed around the 0 ms point, as illustrated in Fig. 3.2. This approach was adopted because the shape of the current curve varies significantly depending on the input voltage and the resulting current. Figure 3.2 depicts the current curve achieved for a 250V input. Additionally the current curve for a 100V input is provided in the Appendix (Fig. A.1).

## 3.2 In situ Diagnostics

### 3.2.1 Ion-current Probe- Langmuir probe

The in-house-built ion collector probe (Figure 3.3) was designed to measure the current density of ions ( $J_i$ ) in ion saturation mode. The probe consisted of a 5 mm diameter copper stick milled down to resemble a nail, it was then covered with Katpon tape to ensure insulation from the holder assembly 3.6.



Figure 3.3: In-house built ion collector probe wrapped in Kapton tape for electrical insulation from the aluminum assembly holder. The probe includes an attachment point for a screw terminal connector, enabling connection to the ion probe circuit (Figure 3.4)

To guarantee full ion collection, the probe was negatively biased at  $V_b = -80$  V, as determined in sec. ??.

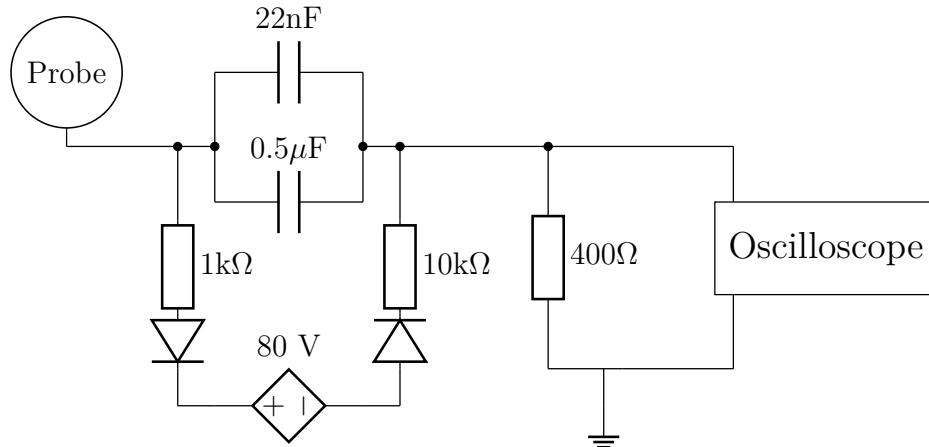


Figure 3.4: Schematic of the ion-flux probe circuit. The  $400\Omega$  resistor converts ion current to voltage, while the  $0.5\mu F$  capacitor and  $400\Omega$  resistor form a high-pass filter with a 795 Hz cutoff.

The circuit incorporates a  $0.5\mu F$  capacitor in series with the  $400\Omega$  resistor, forming a high-pass filter with a cutoff frequency of 795 Hz. This configuration effectively blocks DC and low-frequency noise, ensuring that only plasma fluctuations above 795 Hz are recorded. The high-pass characteristic is essential for isolating the dynamic ion current signal from any static offsets or drift.

To maintain a stable bias voltage, a  $22nF$  capacitor and  $1k\Omega$  resistor are included in the bias supply line. This combination acts as a low-pass filter, smoothing the bias

voltage and minimizing high-frequency ripple.

The processed voltage signal is recorded using a 20 MHz bandwidth oscilloscope. The ion flux  $\Gamma_i$  is then calculated from the recorded voltage  $V$  as:

$$\Gamma_i = \frac{V}{eAR}, \quad (3.2)$$

where  $A = 19.63 \text{ mm}^2$  is the probe area,  $e$  is the elementary charge, and  $R = 400 \Omega$ . This setup ensures accurate measurement of the ion flux while minimizing the impact of noise and DC offsets.

### 3.2.2 Quartz Crystal Microbalance

A quartz crystal microbalance (QCM) was employed to measure the amount of material deposited during cathodic arc sputtering. The configuration used in this work was the INFICON Cool Drawer™ with a single drawer in standard orientation. The sensor is water-cooled to ensure thermal stability, and a 14 mm diameter, 6 MHz AT-cut quartz crystal was operated with a SQM-160 controller for electronic readout.

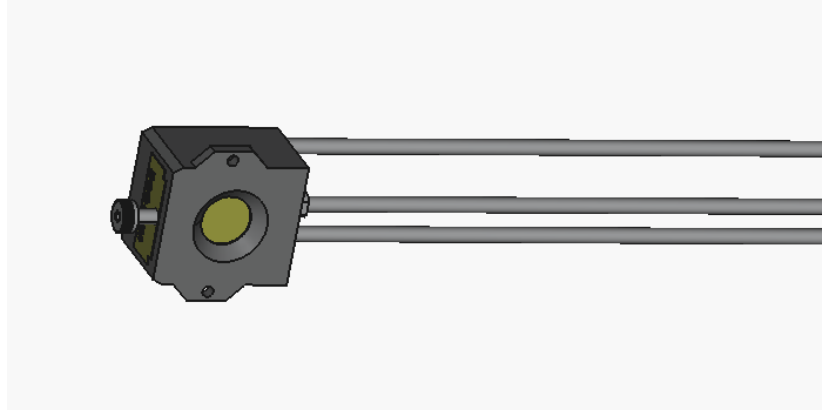


Figure 3.5: Sensor head of the INFICON Cool Drawer™ Quartz Crystal Microbalance (QCM) used for in-situ mass deposition monitoring during cathodic arc sputtering. The assembly includes a water-cooled housing, a 14 mm diameter AT-cut quartz crystal (6 MHz), and electrode leads for connection to the SQM-160 controller. (Schematic adapted from INFICON STP file, available at <https://www.inficon.com/en/products/thin-film-technology/cool-drawer-single-sensor>).

The measurement principle follows the Sauerbrey equation [25], which relates the change in resonance frequency of the quartz crystal to the deposited mass:

$$\Delta m = \frac{N_{\text{AT}} \cdot d_q \cdot \pi r^2}{F_q^2} \cdot \Delta F_c = 18.8146023 \cdot 10^{-9} \frac{g}{Hz} \cdot \Delta F. \quad (3.3)$$

Here  $d_q = 2.649 \frac{\text{g}}{\text{cm}^3}$  is the quartz density, the exposed area of the QCM is  $r = 0.7\text{cm}$ ,  $N_{\text{AT}} = 166\,100 \text{ Hz cm}$  the frequency constant of the AT-cut,  $F_q = 6 \text{ MHz}$  the uncoated resonance frequency, and  $\Delta F$  the measured frequency shift.

The Sauerbrey relation is accurate as long as  $\Delta F \lesssim 0.05F_q$  (about 0.3 MHz for a 6 MHz crystal). For larger mass loadings, the linear approximation fails and the Z-match™ technique is used. This method, introduced by Lu and Lewis in 1972 on the basis of Miller and Bolef's theoretical treatment [20, 17], incorporates the acoustic properties of both the quartz and the deposited film via the acoustic impedance ratio

$$Z = \left( \frac{d_q \mu_q}{d_f \mu_f} \right)^{1/2}, \quad (3.4)$$

with  $d$  and  $\mu$  denoting the density and shear modulus of quartz ( $q$ ) and film ( $f$ ), respectively [13]. In practice, the controller applies a correction function  $f(Z)$  to the Sauerbrey relation,

$$m_f = \frac{N_{\text{AT}} d_q \pi r^2}{F_q^2} \cdot \Delta F \cdot f(Z), \quad (3.5)$$

which compensates for the acoustic mismatch and extends the validity of thickness determination up to  $\sim 0.4F_q$ .

In the present experiments, the observed frequency shifts ranged from about 1 Hz to 50 Hz. With the SQM-160 resolution of approximately 0.03 Hz at 6 MHz, even the smallest shifts were well above the noise floor, yet orders of magnitude below the Sauerbrey breakdown limit. The Sauerbrey approximation was therefore fully sufficient, and Z-match corrections were not required.

### 3.2.3 Comparability with QCM Measurements

The ion collector probe, with its 5 mm diameter, was mounted through a precision-milled pass-through hole in the aluminum mounting block, while the QCM was secured in a dedicated cutout and fixed via screws.

This configuration ensured rigid mechanical alignment between the two diagnostics. The exposed area of the quartz crystal (8 mm diameter) was selected to encompass the probe's collection area, enabling spatially resolved comparisons of ion current density and deposited mass.

This design accounts for the radial gradients in plasma density and ion charge state distribution, which are inherent to expanding cathodic arc plasmas [3, Chap. 6.2]. By positioning the probe right next to the QCM, the ion flux measurements directly reflect

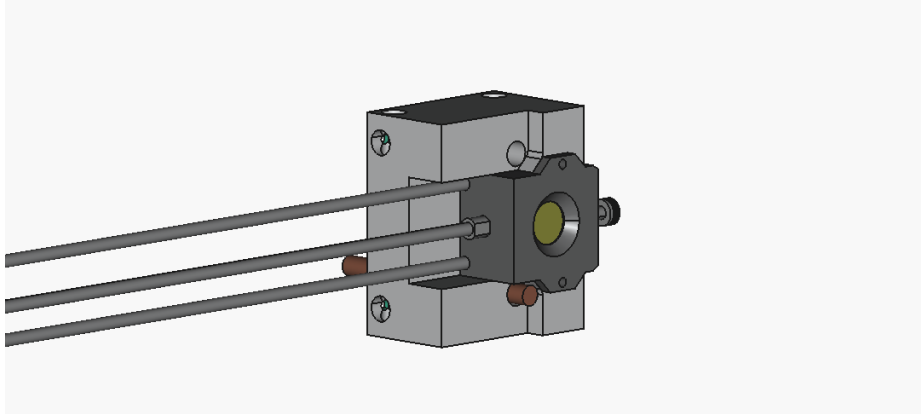


Figure 3.6: Holder Assembly for In-Situ Plasma Diagnostics: Integrated QCMs and Langmuir Ion Collector Probe (interactive 3D model; static preview shown in non-Adobe viewers).

the plasma conditions governing deposition on the crystal surface.

### 3.2.4 Quadrupole Mass Spectrometer

A quadrupole mass spectrometer (QMS, Hiden EQP 1000) was used to measure the ion energy distribution functions (IEDFs) and charge-state-resolved fluxes of plasma species generated during pulsed cathodic arc deposition. The system utilizes an electrostatic energy analyzer with a quadrupole mass filter to separate ions by their kinetic energy and mass-to-charge ratio ( $m/q$ ).

Ions enter the QMS through a 50  $\mu\text{m}$  sampling orifice and are first transported to the energy analyzer, where their kinetic energy  $E_i$  is selected according to the relationship:

$$E_i = \left( V_{\text{ENERGY}} + \frac{R}{d} V_{\text{PLATES}} - V_{\text{AXIS}} \right) n \times e. \quad (3.6)$$

Here,  $V_{\text{ENERGY}}$  and  $V_{\text{AXIS}}$  are opposing potentials applied to the analyzer,  $R$  is the mean radius of the cylindrical sector,  $d$  is the plate separation,  $V_{\text{PLATES}}$  is the potential difference across the sector plates, and  $n \times e$  is the total charge of the ion [11]. The selected ions are then injected into the quadrupole mass filter, where a combination of AC and DC electric fields creates a stability region dependent on  $m/q$ , described by the Mathieu equations [9]. Only ions with trajectories stable in both radial and axial directions reach the detector. The potential in the quadrupole is described by:

$$V(x, y, t) = \frac{U_0 \cos(\omega t)}{r_0^2} (x^2 - y^2), \quad (3.7)$$

where  $U_0$  is the amplitude of the AC voltage,  $\omega$  is the angular frequency, and  $r_0$  is the

field radius. The stability of ion motion is determined by the dimensionless parameters:

$$a = \frac{8eU_{DC}}{mr_0^2\omega^2}, \quad q = \frac{4eU_0}{mr_0^2\omega^2}, \quad (3.8)$$

with  $U_{DC}$  as the superimposed DC voltage. For a given  $m/q$ , stable transmission occurs only within specific  $(a, q)$  regions, enabling mass separation [9, 18].

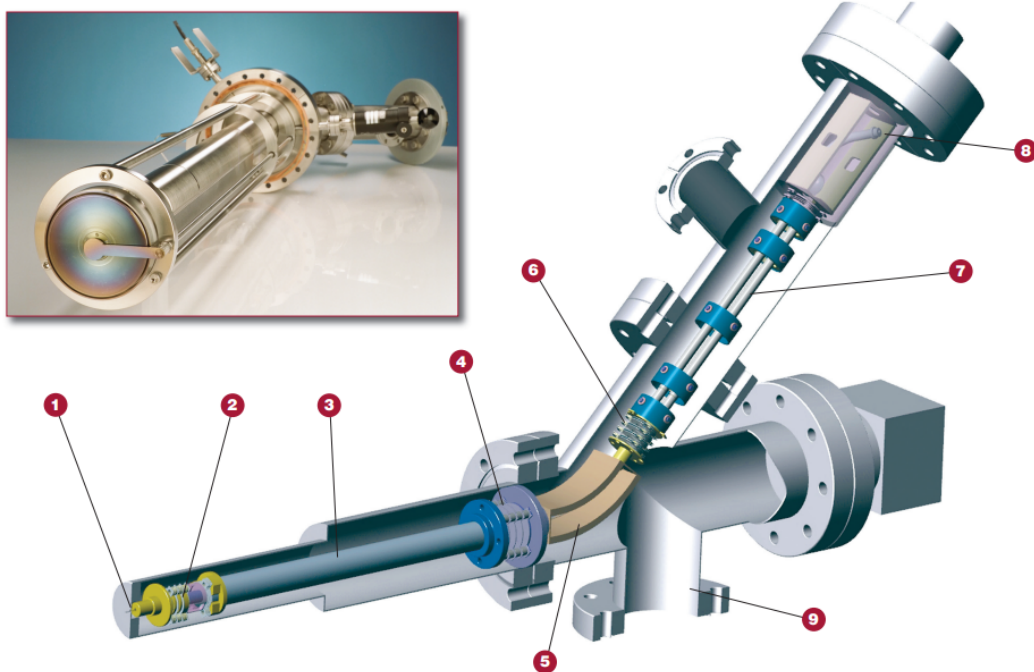


Figure 3.7: ERMS, Hiden EQP HE 1000: (1) Sampling Orifice, (2) Electron Impact Ion Source, (3) Transfer Ion Optics, (4) Quadrupole Lens, (5) Energy Filter, (6) Decelerating Lens, (7) Quadrupole Mass Filter, (8) Detector, (9) Differential Pump Port [1]

To obtain the ion energy distribution functions (IEDFs), the energy-to-charge (E/Q) distributions were measured for different mass-to-charge ratios (M/Q). The energy distributions for ions of different charge states were derived by multiplying the E/Q values by the corresponding charge state number  $Q$ . This correction accounts for the charge-dependent scaling of ion energies.

To reduce interference from the arc's magnetic field, the QMS was equipped with a grounded, mu-metal shield [5].

IEDFs were measured using a double trigger acquisition scheme synchronized with the arc pulses, which had a 1 ms duration and a 5 Hz repetition rate. For each  $m/q$  value, two 20 ms acquisition windows were recorded, activated 10 ms before the onset of the pulse. The combined 40 ms of data for each point were averaged to obtain the final

IEDF. Measurements were performed for charge states  $1^+$ ,  $2^+$ , and  $3^+$  of aluminum ions, and for charge states  $1^+$ ,  $2^+$ ,  $3^+$ , and  $4^+$  of titanium ions. For nitrogen ion species ( $\text{N}$  and  $\text{N}_2$ ), only the  $1^+$  ionization level was measured. This was achieved by scanning  $V_{\text{ENERGY}}$  while fixing the quadrupole mass filter to the corresponding  $m/q$  values.

Ionization	Molar mass over charge ratio of:			
	Al	Ti	N	$\text{N}_2$
$1^+$	27	47.867	14	28
$2^+$	13.5	23.933	-	-
$3^+$	9	15.955	-	-
$4^+$	-	11.966	-	-

### 3.3 Ex situ Measurements

#### 3.3.1 X-ray Diffraction (XRD)

X-ray diffraction (XRD) was employed to analyze the crystallographic structure of the thin films deposited during the experiments. XRD is a non-destructive technique that provides detailed information about the crystalline phases present in the material, as well as their lattice parameters, crystallite size, and strain.

Due to the small film thickness, out-of-plane diffraction techniques were used to enhance the film signal relative to the substrate. Two measurement geometries are employed [21]:

- **Symmetrical reflection ( $2\theta/\theta$  scan):** Both incident and diffracted beams make equal angles with the sample surface. This geometry probes lattice planes parallel to the substrate and is suitable for textured films, but substrate peaks can obscure weak film signals.
- **Asymmetrical reflection (thin-film method):** The incident beam is fixed at a small grazing angle  $\alpha$ , while the detector scans in  $2\theta$ . This reduces the X-ray penetration depth from tens of micrometers to a few micrometers, greatly enhancing sensitivity to thin films [21].

The XRD measurements were performed using a model name of xrd machine diffractometer equipped with non monochromatic  $\text{Cu}_{\text{alpha}}$  source with smt smt wavelength. The asymmetrical reflection scans were performed with an add incidence angle and speed and step size used

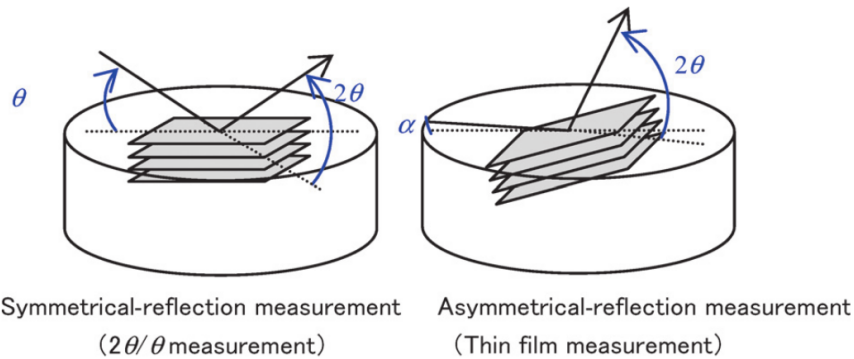


Figure 3.8: Schematic of out-of-plane diffraction geometries: symmetrical reflection (left) and asymmetrical reflection (right) for thin film analysis. Taken from [21].

The crystallographic structure was determined by analyzing the diffraction patterns. The Bragg equation was used to identify the crystalline phases:

$$2d \sin(\theta) = n\lambda, \quad (3.9)$$

where  $d$  is the spacing between atomic planes,  $\theta$  is the diffraction angle,  $n$  is an integer, and  $\lambda$  is the X-ray wavelength.

### 3.3.2 X-ray Reflectometry (XRR)

need to look into before writing about it, more precisely about the specs of the device

### 3.3.3 Scanning Electron Microscopy (SEM)

need to look into before writing about it, more precisely about the specs of the device

### 3.3.4 Energy-dispersive X-ray spectroscopy (EDX)

need to look into before writing about it, more precisely about the specs of the device

### 3.3.5 Profilometry

Stylus profilometry was used to measure film thickness by mechanically tracing the surface topography using a diamond-tipped stylus. The technique provides direct measurement of step heights between masked and deposited regions, making it particularly useful for verifying film thickness values obtained by QCM [23].

In profilometry, a stylus with a small tip radius is dragged across the sample surface with a controlled force of 3 mg while its vertical displacement is monitored electromag-

netically. The resulting trace provides a profile of the surface from which the step height (film thickness) with vertical resolution down to  $\sim 1$  nm can be extracted.

One limitation of contact profilometry is the potential for stylus-induced damage on very soft films, though this was not a concern for the hard TiAlN coatings investigated here. The technique is complementary to XRR, with profilometry providing rapid, direct thickness measurements while XRR offers higher accuracy for very thin films and additional information on density and roughness [29].

## 3.4 Data Processing

Experimental data were processed using custom Python scripts to ensure consistency and reproducibility. A central Excel logbook served as the reference for all measurements, each identified by a unique suffix and linked to its corresponding data files. The logbook recorded experimental parameters such as date, distance, pressures, MFC flow rate, cryopump position, power supply settings, and pulse characteristics, as well as initial and final QCM frequencies for deposited mass determination. Associated oscilloscope waveforms were stored as CSV files for ion current analysis.

A Python script automated data handling by matching logbook entries to raw data, averaging ion current waveforms over multiple pulses to reduce noise when possible, and compiling all parameters into a unified dataset. This ensured uniform processing and efficient preparation for subsequent analysis.

QMS data were evaluated with a separate Python script that integrated raw spectra, applied mass transmission corrections to account for detection biases, and extracted parameters such as mean ion energy, charge state distribution, and potential and kinetic energy components for each species (different ionization levels of the four atoms measured). The processed results were visualized and exported into a structured CSV file for detailed examination of the ion energy distributions.

## 3.5 Error Handling

### 3.5.1 Mass Spectrometry Measurements

In mass spectrometry measurements, particularly in the context of cathodic arc processes, the standard deviation is crucial for characterizing data variability. The non-stationary nature of cathode spots in cathodic arcs leads to significant fluctuations in ion flux and charge composition from pulse to pulse [3]. Calibrating mass spectrometry

measurements can be challenging due to these fluctuations, as random errors at each standard point used to determine the calibration curve can lead to a distribution of values for the same observed response for the unknown [12]. As a result, achieving optimal calibration in such conditions may not be straightforward, and the accuracy of the calibration could be affected.

In this study, while efforts were made to calibrate the mass spectrometer accurately, the inherent difficulties associated with the calibration process in cathodic arc environments suggest that the calibration might not have been optimal. To account for this potential source of error, the impact of truncating the measurement artifact (e.g., signal noise or background interference) at different points was evaluated, and its effect on the data was analyzed in detail. This analysis will be further discussed in Section ??.

As detailed in Appendix B, the standard deviation of energy measurements is calculated using the `calculate_energy_stats` function, providing both average energy and standard deviation. This statistical approach offers a visual representation of measurement variability through error bars. The use of standard deviation in mass spectrometry is well-documented in scientific literature. For instance, standard deviation is commonly used to represent uncertainties in measurements and to describe the scatter among measured data points [7]. This statistical approach is crucial for characterizing data variability and ensuring the accuracy of the measurements.

### 3.5.2 QCM and Ion Current Probe Measurements

For the ion current probe measurements, the standard deviation of the averaged measurements is calculated to characterize the variability in the data. This variability within a pulse can be attributed to several factors: the fluctuations in the plasma potential at the beginning of the pulse, charge exchange reactions between ions and neutrals and variations in the arc current and pulse parameters. These factors can cause fluctuations in the ion current during the pulse, leading to the observed variability [4]. This kind of instability within the pulse will be henceforth shown with the help of error bars.

However, certain sources of error specific to the ion probe must be considered. The design of the ion probe can influence the measurements due to sheath effects, where the sheath around the probe can expand based on the probe's size and the biasing applied [3, Appendix A.2]. Additionally, secondary electron emissions from the probe surface can affect the ion current measurements [3, Chap. 8.2]. These emissions can be caused by interactions between the ions and the probe surface leading to inaccuracies in the measurements. As stated before, each pulse varies in terms of energies and amount of particles; these variations are investigated briefly in Sec. 4.1.4, but cannot

be considered for every data point.

The QCM measurements are subject to inaccuracies in terms of the error in the resonance frequency measurements, which is based on the manufacturer's specifications. The given measurement inaccuracy is  $\Delta f = 0.03$  Hz, which will be taken for error propagation [13]. Additionally, the relative position of the QCM sensor with respect to the ion flux affects the accuracy of the measurements especially at close distances.

### 3.5.3 Error Propagation Analysis

To properly characterize the uncertainties in the derived quantities, a comprehensive error propagation analysis was performed. The primary measured quantities with associated uncertainties are: the ion current  $I_{\text{ion}}$  with standard deviation  $\sigma_I$ , the deposited mass  $m$  measured by QCM with uncertainty  $\sigma_m$ , and the mean charge state  $\bar{Q}$  with standard deviation  $\sigma_Q$  determined from mass spectrometry measurements. These independent measurements are combined to calculate particle fluxes, necessitating careful propagation of uncertainties through the calculation chain.

#### Ion Flux from Current Measurements

The ion flux in mass units  $\Phi_{\text{ion}}$  (in  $\mu\text{g}/\text{cm}^2/\text{s}$ ) is calculated from the measured ion current according to:

$$\Phi_{\text{ion}} = \frac{I_{\text{ion}}}{A \cdot \bar{Q} \cdot e} \quad (3.10)$$

where  $e$  is the elementary charge,  $A$  is the collection area of the ion probe and  $\bar{Q}$  is the mean charge state.

For error propagation, considering the independent uncertainties in  $I_{\text{ion}}$ ,  $\bar{Q}$ , the standard Gaussian error propagation formula gives [26]:

$$\left( \frac{\sigma_{\Phi_{\text{ion}}}}{\Phi_{\text{ion}}} \right)^2 = \left( \frac{\sigma_I}{I_{\text{ion}}} \right)^2 + \left( \frac{\sigma_Q}{\bar{Q}} \right)^2 \quad (3.11)$$

This shows that the relative uncertainties add in quadrature, which is typical for multiplicative error propagation.

#### Atomic Flux from QCM Measurements

The atomic flux  $\Phi_{\text{atom}}$  (in atoms/ $\text{cm}^2/\text{s}$ ) is determined from the mass flux measured by the QCM:

$$\Phi_{\text{atom}} = \frac{\Phi_{\text{mass}} \cdot N_A}{M_{\text{eff}}} \quad (3.12)$$

where  $\Phi_{\text{mass}} = m/(A_{\text{QCM}} \cdot t)$  is the mass flux and  $N_A = 6.022 \times 10^{23} \text{ mol}^{-1}$  is Avogadro's constant. Following the same approach: **this depends what kind of data i get from EDX, else just standard error**

$$\left( \frac{\sigma_{\Phi_{\text{atom}}}}{\Phi_{\text{atom}}} \right)^2 = \left( \frac{\sigma_m}{m} \right)^2 + \left( \frac{\sigma_{M_{\text{eff}}}}{M_{\text{eff}}} \right)^2 \quad (3.13)$$

The QCM mass uncertainty  $\sigma_m$  is calculated from the frequency measurement uncertainty  $\Delta f = 0.03 \text{ Hz}$  using the Sauerbrey relation.

# CHAPTER 4

---

## Results

---

### 4.1 Langmuir Probe Bias Voltage Characterization

#### 4.1.1 Validation of Langmuir Probe Operation

Before plasma diagnostics were performed, the functionality of the custom-built Langmuir probe was verified by checking the characteristic voltage current curve (I-V curve) and fitting it against the theoretical relationship 4.1. Additionally the appropriate negative bias voltage for ion saturation measurements was determined . The aim of this test was to ensure that the probe operates in a regime where the collected current is dominated by ions, excluding contributions from electrons.

The bias voltage tests were performed without nitrogen in the chamber, at a fixed distance of 10 cm from the macroparticle filter, and with an EM coil strength of 0.25 T. Figure 4.1 displays the measured ion current as a function of bias voltage. The blue data points are the experimental results, with the green line shows the exponential saturation fit.

The relationship between the collected current  $I$  and the bias voltage  $V$  was analyzed using the modified Langmuir equation [8]:

$$I = I_{\text{sat}} \left( 1 - e^{\frac{-V}{V_0}} \right) + m \cdot V \quad (4.1)$$

where  $I_{\text{sat}}$  is the saturation current and  $V_0$  is a characteristic voltage. The term  $k$

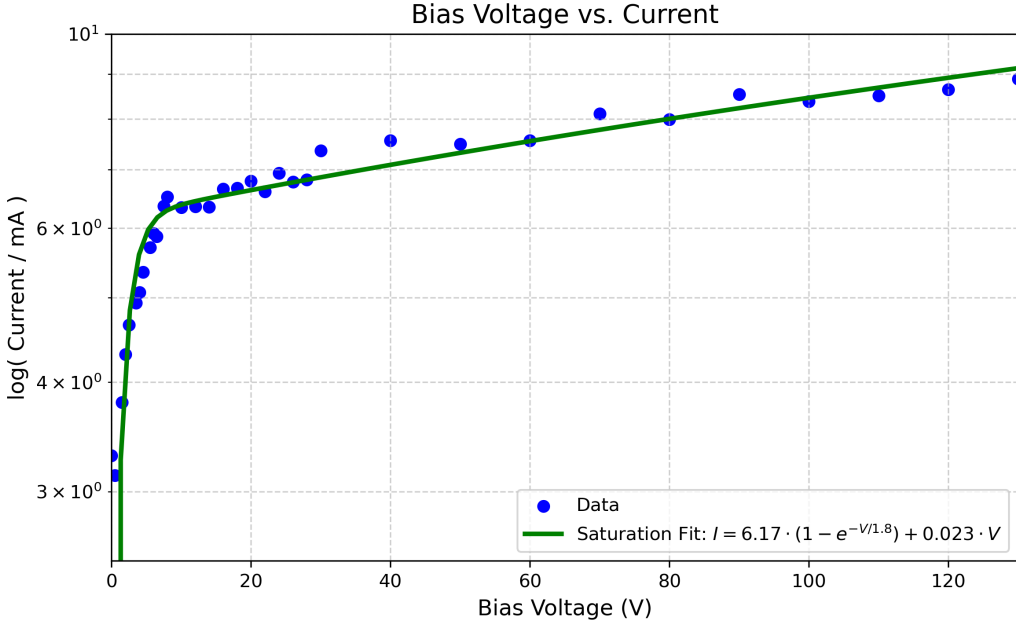


Figure 4.1: Measured ion current vs. bias voltage for the Langmuir probe, showing exponential saturation fit  $I = 6.17 \cdot (1 - e^{-V/1.8}) + 0.023 \cdot V$ . Conditions: no nitrogen, 10 cm from the macroparticle filter, 0.25 T EM-coil strength.

in the equation accounts for plasma sheath expansion and collisional effects at higher bias voltages.

#### 4.1.2 Analysis of the Ion Saturation Curve

As the bias voltage increases, the sheath around the probe grows, which can lead to a non-saturating component in the collected current, this is a common effect seen in small probes. Additionally, collisions within the sheath or presheath region can modify the ion trajectory, resulting in a small linear increase in the collected current with voltage. This correction ensures the model accurately describes the probe's behavior across the full range of applied voltages [8, Chap. 7].

The experimental data were fitted to this equation using a nonlinear least-squares method in Python, yielding the following parameters:

$$I_{sat} = 6.17 \text{ mA}, \quad V_0 = 1.8 \text{ V}, \quad k = 0.023.$$

The bias voltage test results (Figure 4.1) show two distinct regimes:

##### 1. Transition Regime (0 – 40 V):

At low bias voltages the probe collects both ions and electrons. As the negative bias increases, more electrons are repelled, reducing their contribution to the

measured current. This results in a rapid rise in net current as the ion flux begins to dominate. The transition regime is characterized by the decreasing electron flux and the increasing ion flux.

## 2. Saturation Regime (40 – 130V):

Beyond approximately 40V, the current plateaus, indicating that the probe has entered the ion saturation regime. At this point, the negative bias effectively repels all electrons, and the collected current is dominated by ions. However, the current increases slightly with voltage, which is captured by the linear correction term  $k = 0.023$  in the modified Langmuir equation.

### 4.1.3 Selection of Operating Bias Voltage

A bias voltage of -80 V was selected for subsequent measurements to ensure the probe operates well within the ion saturation regime. While the curve begins to saturate around 40 V, choosing a higher voltage provides confidence that the probe is fully repelling electrons and measuring ion flux reliably.

### 4.1.4 Ion current Variation over different pulses

To analyze the pulse-to-pulse variation, approximately 30 single pulses were recorded for each magnetic field strength. The average ion current of each pulse was calculated over the 0–1 ms pulse interval. The final mean and standard deviation were then determined by combining these averages, allowing for an assessment of the differences between pulses. Notably, the 0.05 T data point in Fig. 4.2 includes a significant outlier, with a recorded ion current of approximately 4.8 mA, as detailed in Table 4.1.

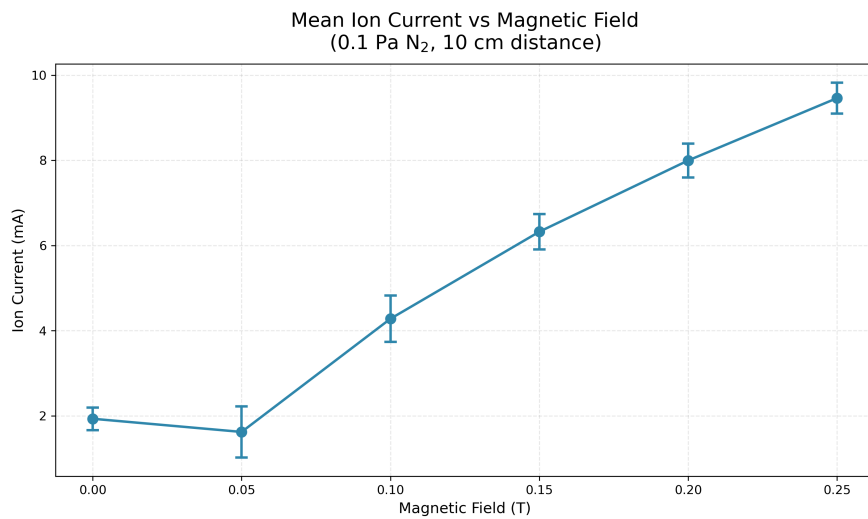


Figure 4.2: Pulse-to-Pulse Variation in Mean Ion Current at Varying Magnetic Fields (0.1 Pa N<sub>2</sub>, 10 cm distance)

EM-coil field (T)	Mean $I_{\text{ion}}$ (mA)	Std (mA)	Std (%)	Range (mA)	# Pulses
0.00	1.931	0.266	13.8	[1.13, 2.26]	30
0.05	1.622	0.602	37.1	[1.16, 4.85]	32
0.10	4.279	0.542	12.7	[2.72, 4.88]	31
0.15	6.323	0.414	6.6	[4.99, 6.92]	27
0.20	7.996	0.399	5.0	[7.26, 8.78]	22
0.25	9.460	0.363	3.8	[8.61, 10.02]	30

Table 4.1: Summary of pulse measurement statistics for varying magnetic field strengths.

In all other measurements, the oscilloscope averaged the voltage drop of the ion current over multiple pulses to produce smoother curves. Therefore, the error reported in subsequent sections primarily reflects variations in ion current within individual pulses, rather than differences between distinct pulses, as previously discussed in Section 3.5.2.

## 4.2 Quartz crystal Microbalance and Ion current Probe

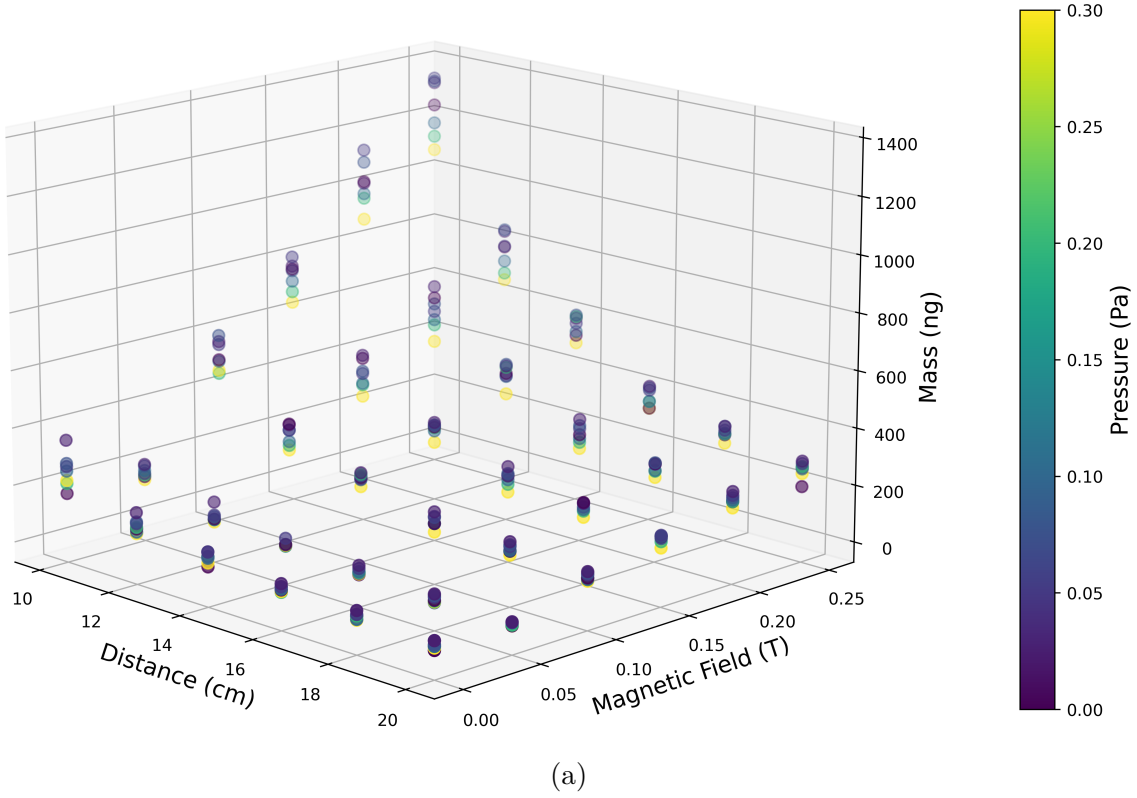
Results will be presented in two subsections for clarity: first, the Quartz Crystal Microbalance (QCM) data, followed by the Ion Current Probe results. This structure is intended to improve the readability and understanding of the trends. At this juncture the quantities of Mass (ng) and Ion current (mA) are not comparable. Overall every permutation of the three parameters in the Table 4.2 were recorded.

Distance (cm)	Pressure (Pa)	Magnetic Field (T)
10	0	0
12	0.025	0.05
14	0.05	0.1
16	0.075	0.15
18	0.1	0.2
20	0.2	0.25
	0.3	

Table 4.2: Parameters used for the QCM/Ion current probe

In Figures 4.3a and 4.3b, a complete overview of the dataset of the deposited masses and the measured ion currents depending on three parameters are shown. These are the distance to the macroparticle filter, the magnetic field strength and the nitrogen background pressure in the chamber. Data points for 0 Pa are in reality more in the order of  $1.5 \cdot 10^{-5}$  Pa.

Mass (ng) vs. Distance (cm), Magnetic Field (T) and Pressure (Pa)



Ion Current (mA) vs. Distance (cm), Magnetic Field (T) and Pressure (Pa)

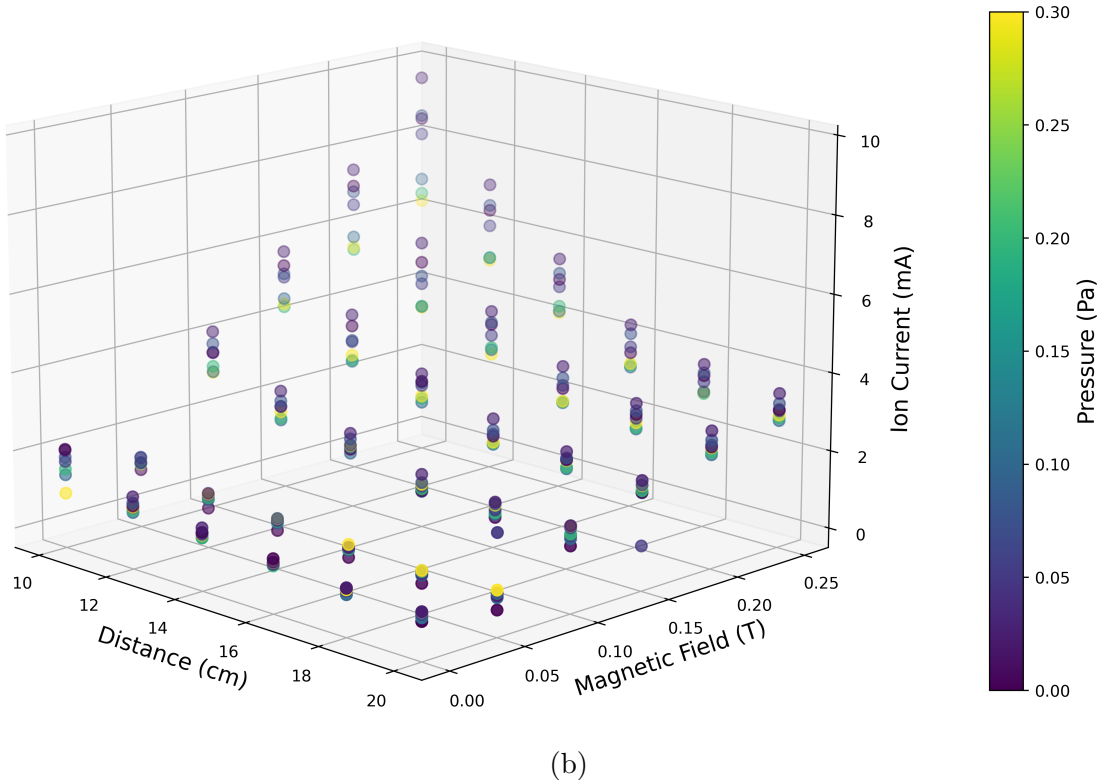


Figure 4.3: (a) The deposited mass (b) The ion current vs. distance, magnetic field strength, and nitrogen background pressure over 64 pulses. Conditions: nitrogen background pressure from 0 Pa to 0.3 Pa, distance from 10 cm to 20 cm from the macroparticle filter, and magnetic field strength from 0 T to 0.25 T.

*Note:* The mass data presented here are based on 64 pulses. This number was chosen because it provides a sufficient mass difference even in the weakest deposition conditions, and it also reduces pulse-to-pulse variability in both the QCM and ion-current probe measurements.

General trends that can be seen already in these figure include:

- The deposited mass and ion current decreases as the distance from the macroparticle filter increases (see Section 4.2.2).
- Higher magnetic field strengths tend to increase the deposited mass and the ion current (see Section 4.2.3).
- The deposited mass shows a complex dependence on nitrogen background pressure. Whereas the ion current seems to be decreasing with increasing nitrogen contents(see Section 4.2.4).

This overview sets the stage for a more detailed analysis of each variable's impact on the deposited mass and ion current. In the following subchapters, we will first examine the metallic case (no nitrogen) with respect to distance and magnetic field strength. Then, we will focus on the specific effects of distance (10 cm, 14 cm and 20 cm), magnetic field strength (0 T, 0.15 T and 0.25 T), and nitrogen background pressure (0.1 Pa and 0.3 Pa) as these are the parameters.

The above stated parameters represent a subset, which as can be seen in Table B.1 include the parameters used in further investigations with ERMS and with deposited films.

### 4.2.1 Metallic Case (No Nitrogen)

In this section, we analyze the deposited mass as a function of distance and magnetic field strength in the absence of nitrogen.

As shown in Figure 4.4, both the deposited mass (after 64 pulses) and the pulse-averaged ion current increase with applied magnetic field. The enhancement is strongest at the shortest distance, indicating that the magnetic field improves plasma focusing and increases the fraction of energetic, highly ionized species reaching the substrate.

At 0.05 T both the ion current and deposited mass fall below the values measured at 0 T. This unexpected drop is likely due to a magnetic mirror effect happening at the coil entrance. As plasma moves from a weak magnetic field into a stronger, the conservation of the particles' magnetic moment causes electrons (which have a lot of perpendicular gyroenergy) to either bounce back or speed up along the field's gradient.

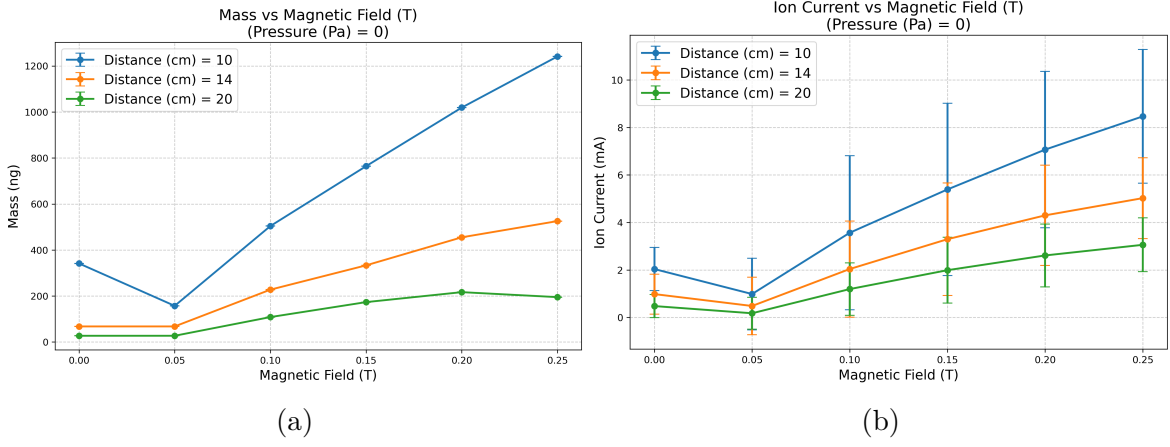


Figure 4.4: Metallic case measurements showing (a) the deposited mass after 64 pulses and (b) the ion current averaged over a single pulse, each plotted as a function of magnetic field strength. Data selected for three distances (10, 14, 20 cm), with error bars representing variation within pulses.

This creates localized space-charge and potential structures that can cut down the overall ion flow further downstream. As a result, you might see a lower ion current and less deposited mass at moderate field strengths, before the effects of focusing and ionization take over at higher fields [3, Chap. 7.6] [10]. This effect is noticeable, in different intensities, in all measurements.

#### 4.2.2 Distance as a variable

In this section, we look at another slice of our dataset looking at the change in mass and ion current vs distance, while taking multiple representative nitrogen pressures (0.1, 0.2, 0.3 Pa) and the metallic case into account at a magnetic field strength of 0.25T.

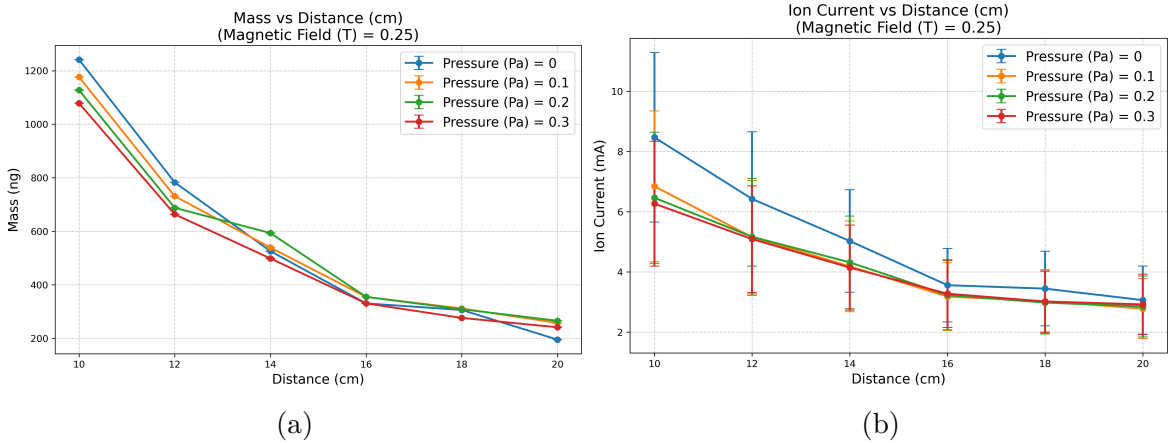


Figure 4.5: QCM and Ion Probe measurements showing (a) the deposited mass after 64 pulses and (b) the ion current averaged over a single pulse, each plotted as a function of distance. Data shown for representative pressures, with error bars representing variation within pulses.

The deposited mass and the ion current both decrease with increasing distance, consistent with the expansion of the plasma. The mass shows a decline with higher chamber pressure resulting in a reduced deposition. In contrast, the ion current exhibits a much steeper drop at short distances, less than 16 cm, when the nitrogen content in the chamber is increased.

This significant change is only present when enhancing the plasma with a magnetic field. In the case like in Fig. A.2, the drop off between metallic and reactive depositions for the ion current is less pronounced, with the ion current being seemingly the same for all pressures at a given distance.

This is in contrast to the measurements done in kalanov paper where reactive had a higher yield, while I get seemingly less or the same mass

#### 4.2.3 Magnetic Field as a variable

here for 14 cm the result is contradictory to the previous statement where added nitrogen leads to higher deposited mass.. funny enough this is the only distance where this is the case as can be seen in fig. 4.6

The next slice of the dataset we take a closer look at is the magnetic field as a variable like in sec. 4.2.1, with the difference being that here the distance is fixed at 14 cm and the nitrogen pressures (0.1, 0.2, 0.3 Pa) and the metallic case are plotted.

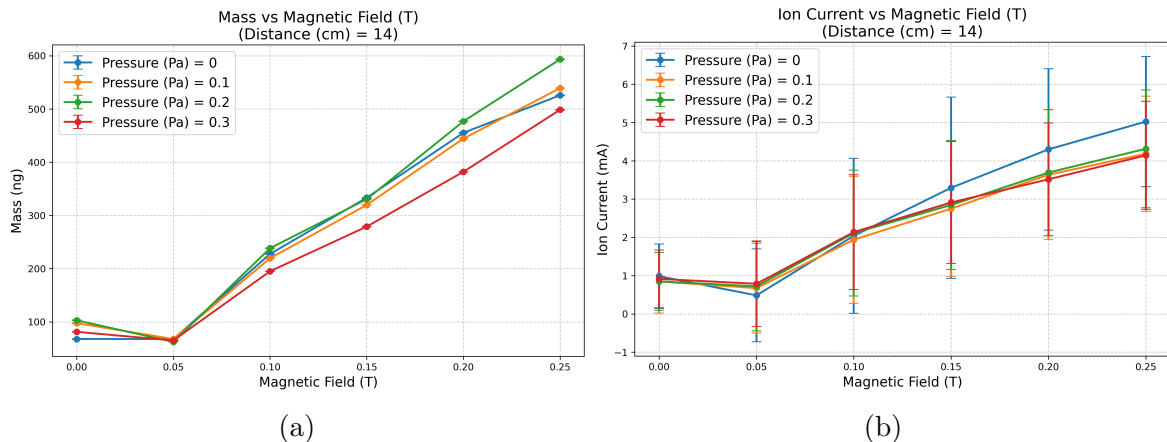


Figure 4.6: QCM and Ion Probe measurements showing (a) the deposited mass after 64 pulses and (b) the ion current averaged over a single pulse, each plotted as a function of Magnetic Field. Data shown for representative pressures, with error bars representing variation within pulses.

In Fig. 4.6, the magnetic-mirror effect is still present, but weaker than in the 10 cm case. At 14 cm, both the deposited mass and the ion current remain essentially constant, whereas at 10 cm a clear decrease was observed, as discussed in subsec. 4.2.1.

The trends observed here suggest that additional nitrogen pressure atmosphere has the smallest influence on the deposited mass compared to distance or the magnetic field. Only for the ion current does the metallic configuration exhibit a slight increase at higher magnetic-field strengths compared to the reactive cases.

#### 4.2.4 Nitrogen pressure as a variable

this could be bc the nitrogen affects plasma trajectory and thus it will measure different masses at differetn pressures, further it makes sense bc at further distances where teh plasma expanded the effect doesnt exist

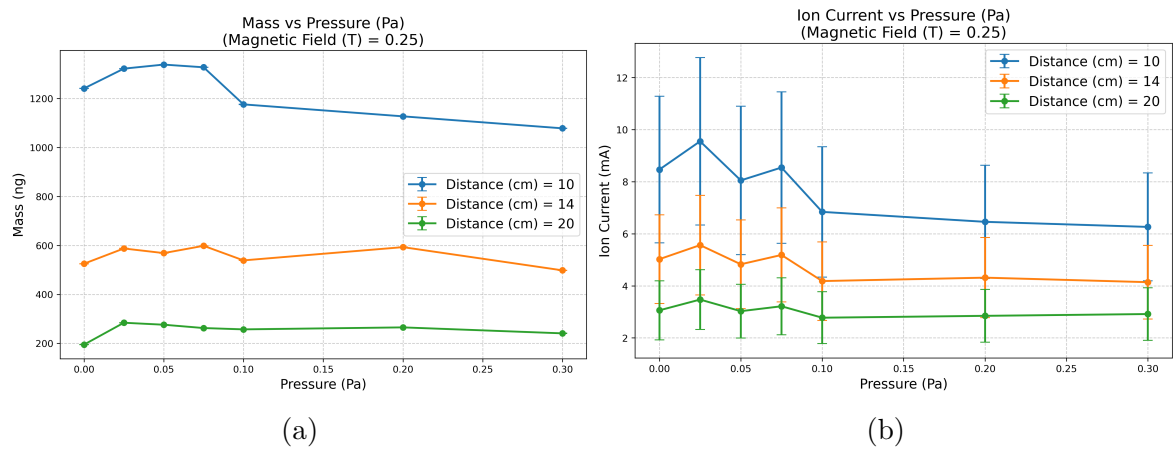


Figure 4.7: QCM and Ion Probe measurements showing (a) the deposited mass after 64 pulses and (b) the ion current averaged over a single pulse, each plotted as a function of Pressure. Data shown for representative pressures, with error bars representing variation within pulses.

### 4.3 Mass spectrometry Results

- shortly about mean charge state and energies not a focus tho
- maybe a table and a picture

Missing 14cm 0.25T

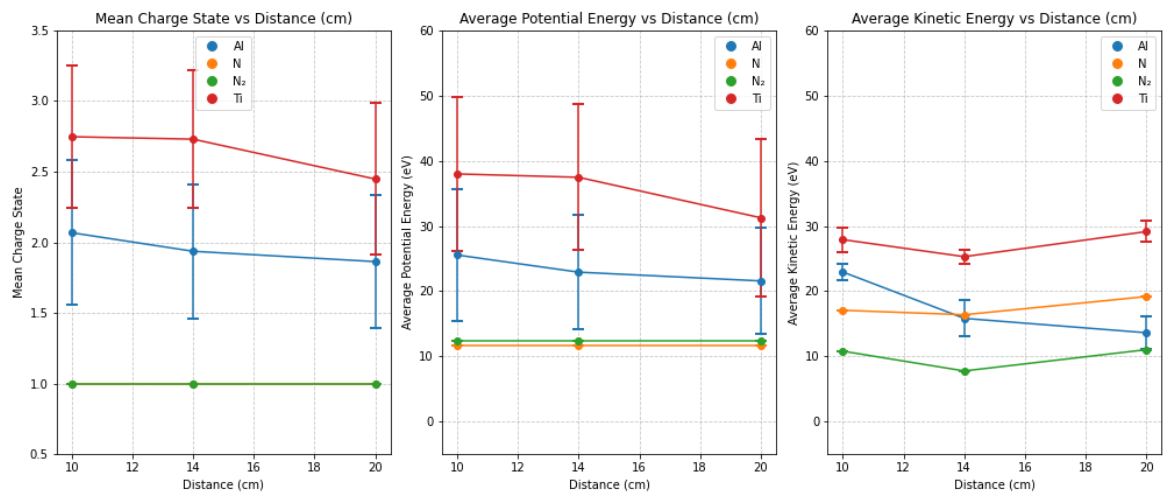


Figure 4.8: 0Pa 0.25T

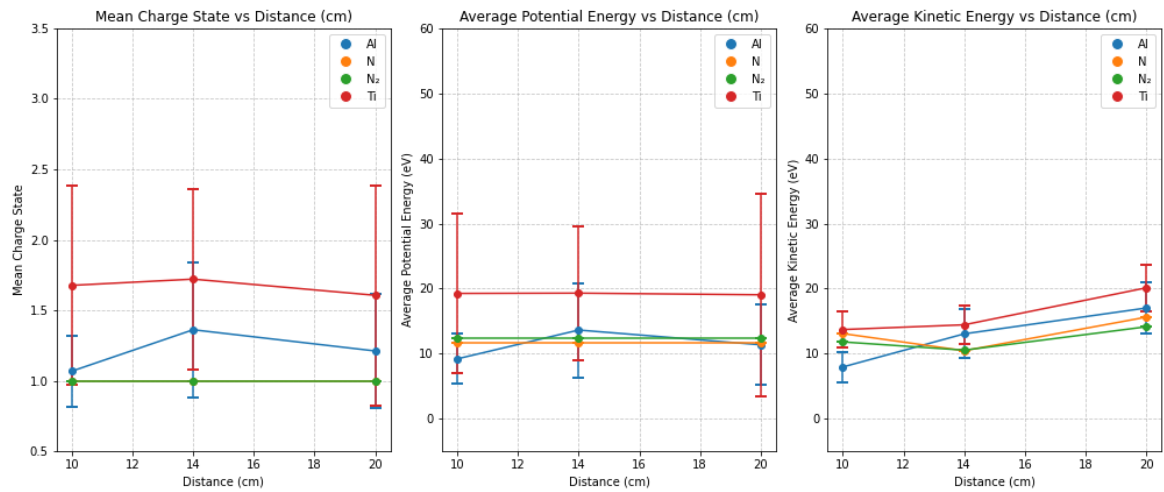


Figure 4.9: 0.3Pa 0.25T

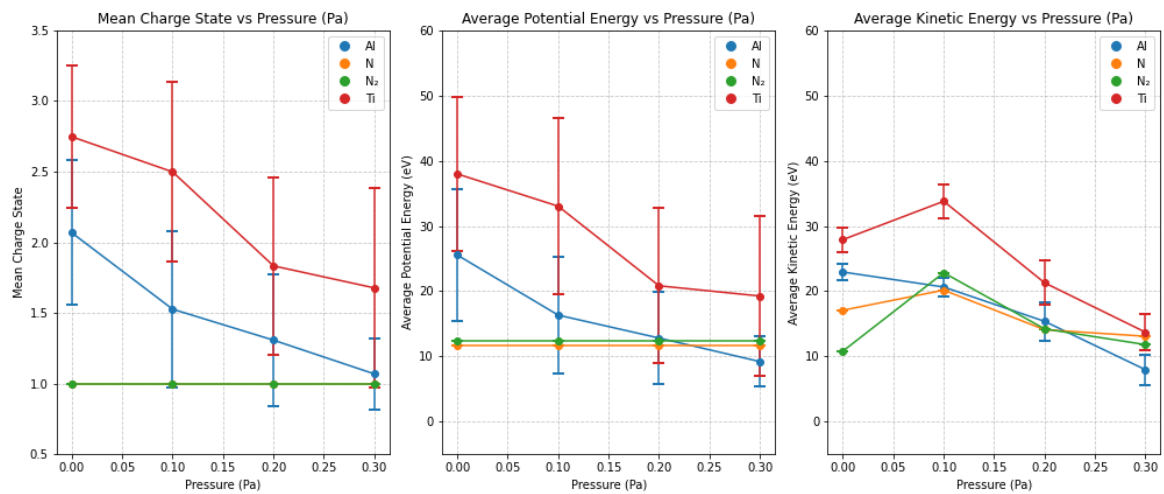
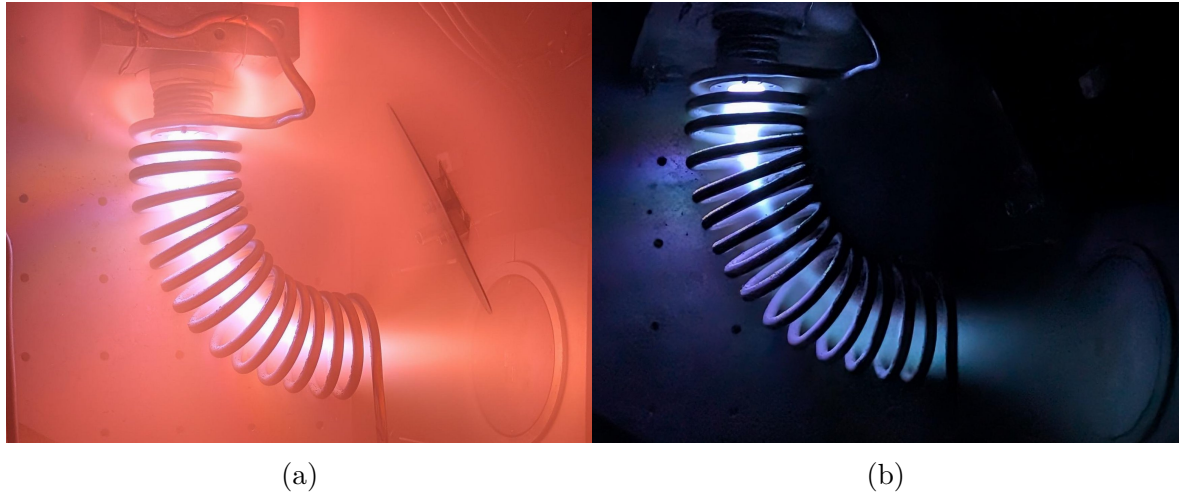


Figure 4.10: 10cm 0.25T

## 4.4 Ex situ Results



(a)

(b)

Figure 4.11: to be written picture taken with phone a) with nitrogen and b) metallic... colors are wrong need to change it haha

A total of [insert number of films once i've done all of them, probably like 6-8] were taking into account for further measurements and looked at in the following sections. Blablabla

### 4.4.1 Profilometry

Samples were prepared by placing a straight marker line near the edge of each substrate prior to deposition. This marker could be cleanly removed by ultrasonic washing after film growth, revealing the deposition step for thickness analysis. Profilometry measurements were performed at three positions on each sample, one near the center and one near each edge. The three measurements were averaged to obtain the mean film thickness. All resulting values are summarized in Table 4.3.

---

Table 4.3: Profilometry thickness measurements for the deposited films

### 4.4.2 XRD

### 4.4.3 XRR

### 4.4.4 EDX

## 4.5 Fluxes

# CHAPTER 5

---

## Discussion of Results

---

Direct comparison between ion current and deposited mass at close distances is complicated due the plasma density gradient

# CHAPTER 6

---

## Conclusion

---

## CHAPTER 7

---

final words or smt like thanks everyone

---

## APPENDIX A

---

### Additional Plots

---

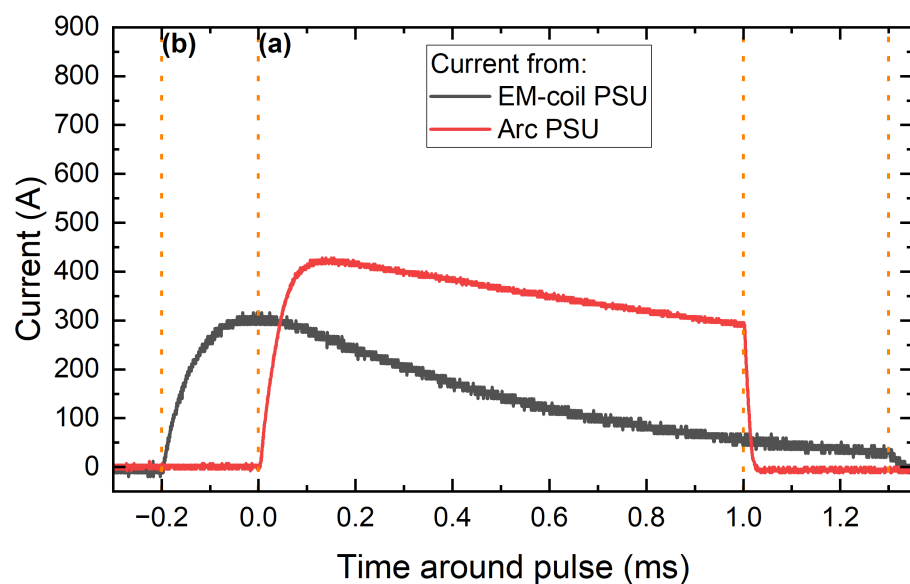
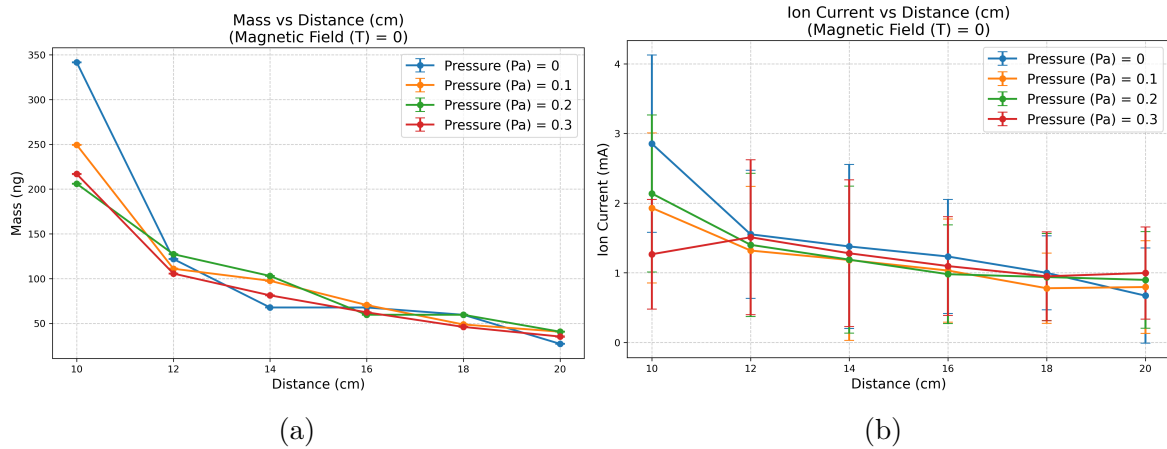


Figure A.1: Additional Pulse waveform with the triggering timings (a) and (b) for the Arc-PSU and the EM-coil PSU marked with the orange dashed line for 100V input



(a)

(b)

Figure A.2: Additional plot for Section 4.2.2. QCM and Ion Probe measurements showing (a) the deposited mass after 64 pulses and (b) the ion current averaged over a single pulse, each plotted as a function of distance. Data shown for representative pressures, with error bars representing variation within pulses.

## APPENDIX B

---

Python code used

---

Table B.1: Complete overview of experimental measurements. All distance/field/pressure combinations not explicitly listed were measured with ion current probe and QCM only. In total: 252 Ion+QCM measurements, 17 ERMS measurements, 6 deposited films

Distance (cm)	Magnetic Field (T)	Pressure (Pa)	Measurements Performed			Film ID
			Ion+QCM	Mass Spec	Ex-situ	
<b>Systematic parameter scan:</b>						
12, 16, 18	0, 0.05, 0.1, 0.15, 0.2, 0.25	0, 0.025, 0.05, 0.075, 0.1, 0.2, 0.3	✓	—	—	—
<b>Distance 10 cm — standard conditions:</b>						
10	0.05, 0.1, 0.2	all pressures <sup>†</sup>	✓	—	—	—
10	0	0.025, 0.05, 0.075, 0.2	✓	—	—	—
10	0.15	0.025, 0.05, 0.075, 0.2	✓	—	—	—
10	0.25	0.025, 0.05, 0.075	✓	—	—	—
<b>Distance 10 cm — with mass spectrometry:</b>						
10	0, 0.15	0, 0.1, 0.3	✓	✓	—	—
10	0.25	0	✓	✓	✓	003
10	0.25	0.1	✓	✓	✓	004
10	0.25	0.2	✓	✓	—	—
10	0.25	0.3	✓	✓	✓	002
<b>Distance 14 cm — standard conditions:</b>						
14	0, 0.05, 0.1, 0.2	all pressures <sup>†</sup>	✓	—	—	—
14	0.15	0, 0.025, 0.05, 0.075, 0.2, 0.3	✓	—	—	—
14	0.25	0.025, 0.05, 0.075, 0.2	✓	—	—	—
<b>Distance 14 cm — with mass spectrometry:</b>						
14	0.15	0.1	✓	✓	—	—
14	0.25	0	✓	✓	✓	008
14	0.25	0.1	✓	(✓)	(✓)	—
14	0.25	0.2	✓	(✓)	(✓)	—
14	0.25	0.3	✓	✓	✓	009
<b>Distance 20 cm — standard conditions:</b>						
20	0, 0.05, 0.1, 0.15, 0.2	all pressures <sup>†</sup>	✓	—	—	—
20	0.25	0.025, 0.05, 0.075, 0.1, 0.2	✓	—	—	—
<b>Distance 20 cm — with mass spectrometry:</b>						
20	0.25	0, 0.3	✓	✓	—	—

<sup>†</sup>all pressures = 0, 0.025, 0.05, 0.075, 0.1, 0.2, 0.3 Pa

Ion+QCM: Ion current probe and quartz crystal microbalance (in situ)

Mass Spec: Energy-resolved mass spectrometry (ERMS)

Ex-situ: XRD, SEM, profilometry characterization of deposited films

---

## Bibliography

---

- [1] Hiden Analytical. EQP: Mass and Energy Analyser for plasma diagnostics. [https://www.hidenanalytical.com/wp-content/uploads/2016/08/EQP-poster\\_A1\\_print.pdf](https://www.hidenanalytical.com/wp-content/uploads/2016/08/EQP-poster_A1_print.pdf), 2016. [Accessed 18-11-2025].
- [2] André Anders. A structure zone diagram including plasma-based deposition and ion etching. *Thin Solid Films*, 518(15):4087–4090, 2010.
- [3] André Anders. *Cathodic arcs: from fractal spots to energetic condensation*, volume 50. Springer, 2008.
- [4] André Anders. The evolution of ion charge states in cathodic vacuum arc plasmas: a review. *Plasma Sources Science and Technology*, 2012. A review article that discusses various factors influencing ion charge states in cathodic vacuum arc plasmas.
- [5] André Anders and George Yu Yushkov. Ion flux from vacuum arc cathode spots in the absence and presence of a magnetic field. *Journal of Applied Physics*, 91(8):4824–4832, 2002.
- [6] J. Benedikt and A. Kersten, H. and Henning. Quadrupole mass spectrometry of reactive plasmas. *Journal of Physics D: Applied Physics*, 40(20):6300–6316, 2007.
- [7] R. L. Boxman, S. Goldsmith, and D. M. Sanders. Cathodic arc plasmas and their applications. *IEEE Transactions on Plasma Science*, 23(6):939–956, 1995. Includes quantitative plasma diagnostics where standard deviation is used to characterize measurement scatter and reproducibility of arc plasma parameters.
- [8] Francis F. Chen. *Introduction to Plasma Physics and Controlled Fusion*, volume 1. Springer, New York, 1984.

- [9] P. H. Dawson. *Quadrupole Mass Spectrometry and Its Applications*. IM Publications, Chichester, UK, 1997.
- [10] Luis Fernández, José Torres, Octavio Gómez, and Eduardo Tirado Bueno. Charged particle reflection in a magnetic mirror. *Revista Mexicana de Física E*, 21, 07 2024.
- [11] Hiden Analytical, Warrington, UK. *EQP Technical Manual: Energy-Resolving Quadrupole Mass Spectrometer*, 2024.
- [12] A. Hubaux and G. Vos. Quantitative mass spectrometry: Part ii. *Anal. Chem.*, 42(8):849, 1970.
- [13] INFICON, Bad Ragaz, Switzerland. *SQM-160 Multi-Film Rate/Thickness Monitor Operating Manual*, 2015. PN 074-511-P1E.
- [14] Burkhard Jüttner. Cathode spots of electric arcs. *Journal of Physics D: Applied Physics*, 34(17):R103–R123, 2001.
- [15] Dmitry Kalanov, Slavi Mandazhiev, Julius Franze, André Anders, and Yeliz Unutulmazsoy. Decoupling the effects of potential energy, kinetic energy, and ion flux on crystallinity of v-al and v-al-n thin films in pulsed filtered cathodic arc deposition. *Surface and Coatings Technology*, 497, 2025.
- [16] Soheil Karimi Aghda, Alireza Alyani, Frans Munnik, Maren Keunecke, Marcus Hans, Daniel Primetzhofer, and Jochen M. Schneider. Ion kinetic energy- and ion flux-dependent mechanical properties and thermal stability of (ti,al)<sub>n</sub> thin films. *Acta Materialia*, 251:118897, 2023.
- [17] C. Lu and O. Lewis. Investigation of film-thickness determination by oscillating quartz resonators with large mass load. *Journal of Applied Physics*, 43(11):4385–4390, 1972.
- [18] R. E. March and R. J. Hughes. *Quadrupole Storage Mass Spectrometry*. Wiley, 1989.
- [19] P. H. Mayrhofer, D. Music, and J. M. Schneider. Ab initio calculated binodal and spinodal of cubic  $\text{ti}_{1-x}\text{al}_x\text{n}$ . *Applied Physics Letters*, 88(7):071922, 2006.
- [20] R. E. Miller and D. I. Bolef. Shear modulus and internal friction in single-crystal quartz at low temperatures. *Journal of Applied Physics*, 39(11):5815–5821, 1968.
- [21] Toru Mitsunaga. X-ray thin-film measurement techniques ii. out-of-plane diffraction measurements. *The Rigaku Journal*, 25(1):7–12, 2009.

- [22] S. Paldey and S. C. Deevi. Single layer and multilayer wear resistant coatings of (ti,al)n: a review. *Materials Science and Engineering: A*, 342(1–2):58–79, 2003.
- [23] C. Y. Poon and B. Bhushan. *Comparison of surface roughness measurements by stylus profiler, AFM and non-contact optical profiler*, volume 190. 1995.
- [24] R. Rachbauer, S. Massl, E. Pogatscher, H.-P. Strunk, and P. H. Mayrhofer. Decomposition pathways in age hardening of ti-al-n films. *Journal of Applied Physics*, 110(2):023515, 2011.
- [25] Günter Sauerbrey. Verwendung von schwingquarzen zur wägung dünner schichten und zur mikrowägung. *Zeitschrift für Physik*, 155(2):206–222, Apr 1959.
- [26] John R. Taylor. *An Introduction to Error Analysis: The Study of Uncertainties in Physical Measurements*. University Science Books, Sausalito, CA, 2nd edition, 1997.
- [27] John A. Thornton. High rate thick film growth. *Annual Review of Materials Science*, 7:239–260, 1977.
- [28] Yeliz Unutulmazsoy, Dmitry Kalanov, Kyunghwan Oh, Soheil Karimi Aghda, Jürgen W. Gerlach, Nils Braun, Frans Munnik, Andriy Lotnyk, Jochen M. Schneider, and André Anders. Toward decoupling the effects of kinetic and potential ion energies: Ion flux dependent structural properties of thin (v,al)n films deposited by pulsed filtered cathodic arc. *Journal of Vacuum Science & Technology A*, 41(6), 2023.
- [29] D. Windover, K. M. Gaff, D. Lee, and M. J. Dalberth. Profilometry and atomic force microscopy for surface characterization. *Materials Characterization*, 43(5):347–355, 1999.